Simulations of Polarimetric, X-Band Radar Signatures in Supercells. Part I: Description of Experiment and Simulated ρ_{hv} Rings

JEFFREY C. SNYDER

Cooperative Institute for Mesoscale Meteorological Studies, University of Oklahoma, and NOAA/OAR/National Severe Storms Laboratory, and School of Meteorology, University of Oklahoma, Norman, Oklahoma

HOWARD B. BLUESTEIN

School of Meteorology, University of Oklahoma, Norman, Oklahoma

DANIEL T. DAWSON II

Purdue University, West Lafayette, Indiana

YOUNGSUN JUNG

Center for Analysis and Prediction of Storms, Norman, Oklahoma

(Manuscript received 5 April 2016, in final form 26 April 2017)

ABSTRACT

With the development of multimoment bulk microphysical schemes and polarimetric radar forward operators, one can better examine convective storms simulated in high-resolution numerical models from a simulated polarimetric radar perspective. Subsequently, relationships between observable and unobservable quantities can be examined that may provide useful information about storm intensity and organization that otherwise would be difficult to obtain. This paper, Part I of a two-part sequence, describes the bulk microphysics scheme, polarimetric radar forward operator, and numerical model configuration used to simulate supercells in eight idealized, horizontally homogenous environments with different wind profiles. The microphysical structure and evolution of copolar cross-correlation coefficient (ρ_{hv}) rings associated with simulated supercells are examined in Part I, whereas Part II examines Z_{DR} columns, Z_{DR} rings, and K_{DP} columns. In both papers, some systematic differences between the signature seen at X and S bands are discussed. The presence of hail is found to affect ρ_{hv} much more at X band than at S band (and is found to affect Z_{DR} more at S band than at X band), which corroborates observations. The ρ_{hv} half ring is found to be associated with the presence of large, sometimes wet, hail aloft, with an ~20-min time lag between increases in the size of the ρ_{hv} ring aloft and the occurrence of a large amount of hail near the ground in some simulations.

1. Introduction

Substantial knowledge of the structure and evolution of severe convective storms has been gained from the results of early numerical simulations by Klemp and Wilhelmson (1978), Rotunno (1981), Klemp et al. (1981), Weisman and Klemp (1982), Klemp and Rotunno (1983), and many others. Most of the previous work (e.g., Wicker and Wilhelmson 1995; Adlerman and Droegemeier 2002, 2005; Van Den Broeke et al. 2010), however, examined simulated convective storms from a

kinematic, thermodynamic, dynamic, and microphysical perspective, but validating model microphysics in particular has been hampered by the relative dearth of observations. Obtaining detailed in situ observations of the thermodynamic and microphysical structure of convective storms, particularly above 2–10 m AGL, has proven difficult owing to the limited number of instruments capable of collecting such data and the danger of data collection near and within intense convective storms such as supercells. Polarimetric radars, however, can sample convective storms with much higher spatiotemporal coverage than can many in situ platforms. Since the types and distributions of hydrometeors directly affect

Corresponding author: Jeffrey Snyder, jeffrey.snyder@noaa.gov

polarimetric radar quantities, the structure and evolution of the radar fields can provide important insight into the underlying microphysical and dynamical processes that are otherwise difficult to observe in supercells (e.g., Kumjian and Ryzhkov 2008, hereinafter KR08; Picca and Ryzhkov 2012; Snyder et al. 2013). For example, regions of very low copolar cross-correlation coefficient (ρ_{hv})[1] above the environmental 0°C level may be associated with large hail growth. Subsequently, the structure and evolution of this feature may provide insight into the potential for large hail falling to the ground (e.g., Picca and Ryzhkov 2012). Similarly, changes in the height of a differential reflectivity (Z_{DR}) column (an upward extension of positive Z_{DR} associated with the updrafts of convective storms that has been observed to extend substantially above the 0°C level) may be an indication of updraft intensity changes (e.g., KR08; Kumjian et al. 2014; Snyder et al. 2015).

Despite the fact that most microphysics schemes do not provide all of the necessary information required to calculate scattering amplitudes and polarimetric quantities precisely (nearly all schemes do not allow hydrometeor densities to vary, predict hydrometeor shape, predict liquid water fraction, predict water distribution within mixed-phase hydrometeors, etc.), recent attempts to simulate the polarimetric structure of convective storms have provided realistic-looking radar fields (e.g., Jung et al. 2010; Ryzhkov et al. 2011; Dawson et al. 2014; Johnson et al. 2016). Modeling of microphysical processes that occur within convective storms has improved with the development of multimoment bulk microphysical schemes (e.g., Milbrandt and Yau 2005a,b; Morrison et al. 2005; Mansell et al. 2010), and the emergence of polarimetric radar forward operators (PRFOs; e.g., Pfeifer et al. 2008; Jung et al. 2008, 2010; Ryzhkov et al. 2011; Dawson et al. 2014; Posselt et al. 2015) lets us examine simulated convective storms using quantities that are readily observable by radar. Since operational meteorologists use information from weather radars when assessing threats associated with severe convective storms, it is beneficial to be able to diagnose (and predict) unobservable storm characteristics using observed radar data. Fully acknowledging the shortcomings of bulk microphysics schemes, the motivation of this study is to examine, using a PRFO, the relationship between polarimetric structures and their microphysical characterizations within simulated supercells. This study builds upon the results of Jung et al. (2010), who focused

primarily on comparing simulated polarimetric signatures produced with a double-moment microphysics scheme with those from a single-moment microphysics scheme. Herein, we use a three-moment microphysics scheme on a higher-resolution grid to examine several of the signatures in more detail using multiple simulations.

There are three primary sets of questions examined in this two-part series:

1) Can the model and forward operator reproduce previously identified polarimetric signatures such as ρ_{hv} rings and K_{DP} and Z_{DR} columns?
2) What is the microphysical composition of forward-simulated ρ_{hv} rings, Z_{DR} columns and rings, and K_{DP} columns? How is the appearance of these signatures affected by radar wavelength?
3) What correlations exist between the radar variables and underlying processes that can allow us to infer storm characteristics from radar data? Are there prognostic tendencies to indicate that changes in the structure or evolution of the simulated polarimetric signatures can be used to infer changes to supercell structure?

The majority of the results presented herein and the accompanying discussion will address the polarimetric representation as seen by a radar operating at X band (i.e., radar wavelength $\lambda \approx 3.2$ cm). Despite there being an increasing number of polarimetric X-band radars in use (e.g., Anagnostou et al. 2006; Bluestein et al. 2007a,b; Pereira Filho et al. 2007; Maki et al. 2008; McLaughlin et al. 2009; Asefi-Najafabady et al. 2010; Burgess et al. 2010; Bharadwaj et al. 2011; Bechini et al. 2013; Junyent et al. 2013; Pazmany et al. 2013; Wurman et al. 2014), the majority of previous studies of the polarimetric structure of supercells used data collected at S band; specific attention to X-band radar signatures in supercells is warranted owing to the increasing popularity of X-band radars. Although attenuation at X band is typically much greater than it is at S band, X-band radars have several advantages over those that operate at longer wavelengths. For example, X-band radars can use smaller antennas for a desired half-power beamwidth (which aids deployment and transportability and reduces costs). In addition, at least one very relevant polarimetric quantity (specific differential phase K_{DP}) is generally much more useful (particularly in areas of low rainwater content) at X band than it is at S and C bands.

Where possible, observations collected by polarimetric, X-band, mobile radars to which the authors have access will be shown. Unfortunately, most of the data that the authors have collected do not extend high enough into the convective storms to sample the signatures examined herein adequately because the focus of

---

[1] In common meteorological usage, the relevant quantity is actually the magnitude of ρ_{hv} at lag 0 [i.e., $|\rho_{hv}(0)|$]. For simplicity, this quantity will be referred to solely as ρ_{hv}.

data collection frequently was on the low-level mesocyclone and any tornado that may be occurring. In addition, there are often complicating artifacts that detrimentally impact data analysis for those datasets that do contain these signatures. Artifacts that are commonly observed to degrade ρ_{hv} include nonuniform beamfilling (e.g., Ryzhkov 2007), low signal-to-noise ratio bias, and three-body scatter signatures (or ''hail spikes''; e.g., Zrnić 1987; Wilson and Reum 1988; Hubbert and Bringi 2000). Highly anomalous attenuation and different attenuation are also often seen, as are biases owing to cross coupling that occurs in regions of ice with nonzero mean canting angles (e.g., Ryzhkov and Zrnić 2007; Hubbert et al. 2010a,b, 2014). Many of these artifacts are present in S- and C-band data as well, though some artifacts may be more evident at X band. Regardless, they can complicate analysis unless they are accounted for.

The scattering properties of hydrometeors can vary by radar wavelength on account of resonance effects associated with non-Rayleigh scattering. The scattering characteristics of hail, in particular, can vary widely depending upon radar frequency. It is important to consider these differences if one is familiar only with radar characteristics of precipitation at a particular wavelength. In addition, these differences themselves provide some of the motivation to study polarimetric signatures at X band because their appearances can, at times, be quite different at two different radar wavelengths. An example of how the appearance of hail varies by radar wavelength using polarimetric radar data collected at S and X bands is provided in Fig. 1. The hail core of a supercell that occurred on the afternoon of 17 April 2013 in southwestern Oklahoma was sampled well by the Frederick, Oklahoma, ''KFDR'' S-band Weather Surveillance Radar-1988 Doppler (WSR-88D), at a range of approximately 45–50 km, and the mobile rapid-scan X-band polarimetric radar known as ''RaXPol'' (Pazmany et al. 2013), at a range of approximately 15–20 km (Fig. 1). Several minutes before these data were collected, hail of ~4.5 cm in diameter was reported (National Climatic Data Center 2013). As seen in Fig. 1, attenuation-corrected Z_H is considerably lower, Z_{DR} is considerably higher, and ρ_{hv} is considerably lower in the RaXPol observations relative to the KFDR observations. Most polarimetric attenuation estimation methods (e.g., Bringi et al. 1990, 2001; Zrnić and Ryzhkov 1996; Smyth and Illingworth 1998; Testud et al. 2000; Anagnostou et al. 2004; Gorgucci and Chandrasekar 2005; Park et al. 2005a,b; Ryzhkov et al. 2007; Snyder et al. 2010) rely upon some sort of relationship between specific attenuation (A_H), specific differential attenuation (A_{DP}), and K_{DP}, and nearly all have been developed for attenuation through rain. In this case, K_{DP} in

the hail region (not shown) is ~0° km^{-1}; one can infer the presence of hydrometeors other than raindrops (e.g., hail) where this anomalously strong differential attenuation is undercorrected. Whereas evidence of the hail in ρ_{hv} from KFDR is less distinct, there is a large reduction in Z_{DR}, a tendency that is nearly opposite that seen in the RaXPol observations. The differences between the S- and X-band data are consistent with expectations based upon scattering simulations (e.g., Dolan and Rutledge 2009).

Part I of this paper presents details of the numerical model, bulk microphysics scheme, and PRFO used in this study. Subsequent to such details, one prominent polarimetric signature identified in previous observations of supercells—the ρ_{hv} ring—is examined. These ρ_{hv} rings are circular or semicircular areas of reduced ρ_{hv} observed in the midlevels of supercells. In the cases where the reduced ρ_{hv} appears only as a half ring, it is located along or near the north and east (i.e., downshear) sides of the midlevel updraft (KR08; Payne et al. 2010). KR08 and Kumjian (2013b) speculate that the ρ_{hv} ring consists of mixed-phase hydrometeors of varying size, shape, and dielectric constant falling in or along the periphery of the updraft. In observations analyzed by Payne et al. (2010), a ρ_{hv} ring in a supercell was located in proximity to the vertical vorticity maximum within the mesocyclone, leading them to hypothesize that the flow around the mesocyclone affected the trajectories of mixed-phase hydrometeors such that a ring or half ring appeared. This feature is worthy of study because it may provide some insight into mesocyclone evolution and may aid the identification of large hail (and its growth) aloft. Regarding the latter, Picca and Ryzhkov (2012) found that large reductions in ρ_{hv} were observed before very large hail was observed at the surface; observations from two polarimetric radars indicated that the amount of reduction in ρ_{hv} may be directly related to hail size. The microphysical composition of ρ_{hv} rings simulated and reported on in this paper will be examined to assess the degree to which these high-resolution numerical simulations corroborate the previous discussions of this feature. In addition, although this paper will focus primarily on signatures at X band, we will point out where there are substantial differences in the appearance of particular signatures (especially ρ_{hv} rings, which seem to be the most sensitive to radar wavelength) at X and S bands. Again, since most of the existing literature addressing polarimetric signatures such as ρ_{hv} rings used data from S-band radars, we feel it is important to make special note where simulated polarimetric signatures differ substantially at X band.

Snyder et al. (2017, hereinafter Part II) examine additional polarimetric signatures that have been observed
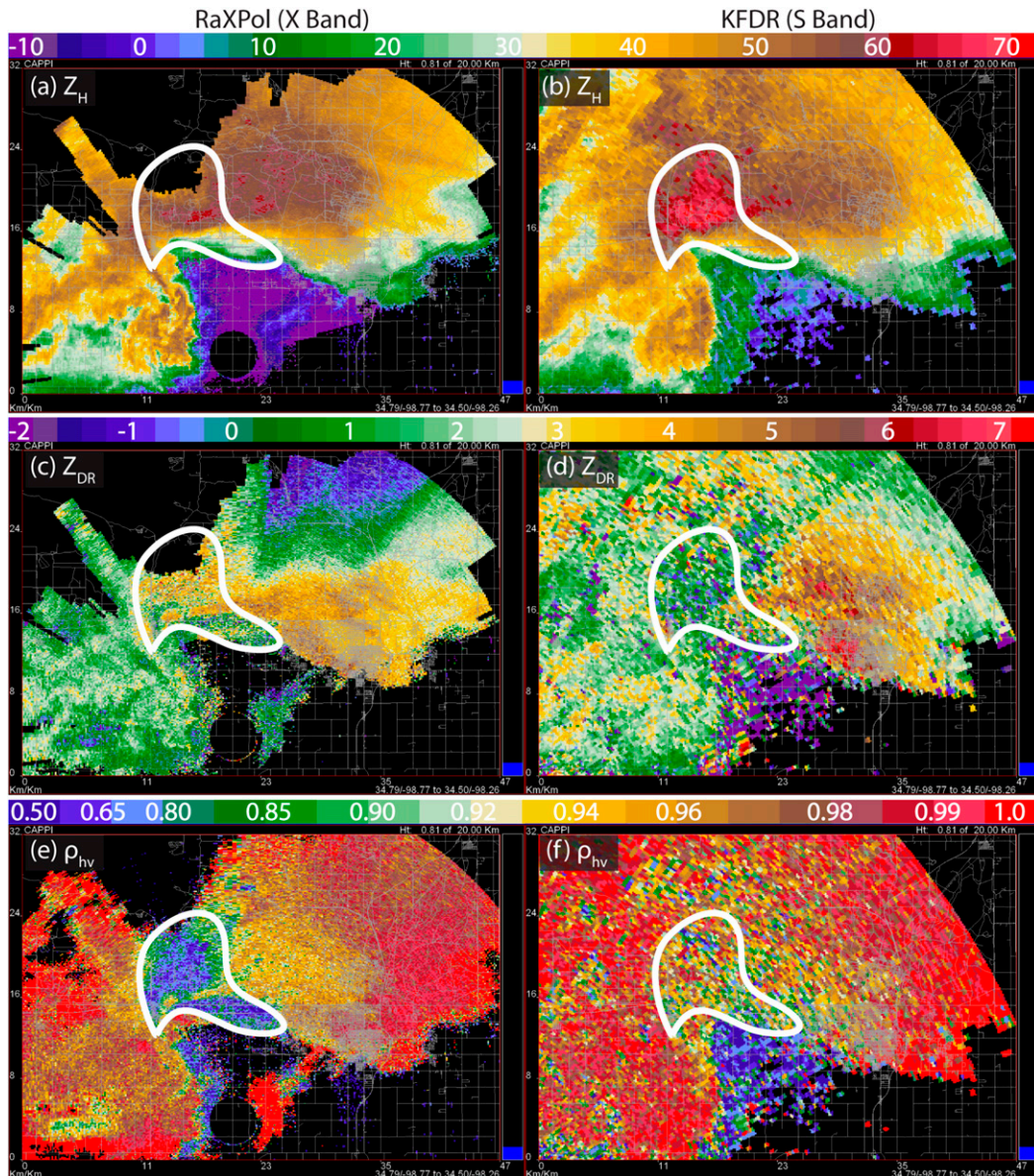
FIG. 1. Images of (a),(b) Z_H, (c),(d) Z_{DR}, and (e),(f) ρ_{hv} from (left) RaXPol (X band) and (right) KFDR (S band) from 2217 UTC 17 Apr 2013. This supercell produced hail of at least 44 mm in diameter near this time. The white outlines in all panels mark areas of RaXPol $\rho_{hv} < 0.8$. The hail signature is seen most prominently in Z_H and Z_{DR} at S band and in ρ_{hv} at X band. Local roads are show in light gray, and most areas feature roads on a grid with a spacing of approximately 1.6 km. The scale of all panels is the same. The effects of attenuation through rainfall have been estimated and compensated for in (a) using the ZPHI method (Testud et al. 2000; Snyder et al. 2010); differential attenuation has been estimated and compensated for in (c) using a relation between attenuation and differential attenuation valid in rain. Anomalous differential attenuation is evident to the northeast of the black outline in (b).

in supercells. In particular, Part II examines the structure and evolution of simulated Z_{DR} and K_{DP} columns and Z_{DR} rings. An example of these "midstorm" polarimetric signatures associated with the simulated supercells that are examined in the two parts of this paper is shown in Fig. 2.

2. Methods and tools

a. Multimoment bulk microphysics

Hydrometeor particle size distributions (PSDs) often are well fit by a gamma distribution (e.g., Ulbrich 1983; Mallet and Barthes 2009). As in Ulbrich (1983) and
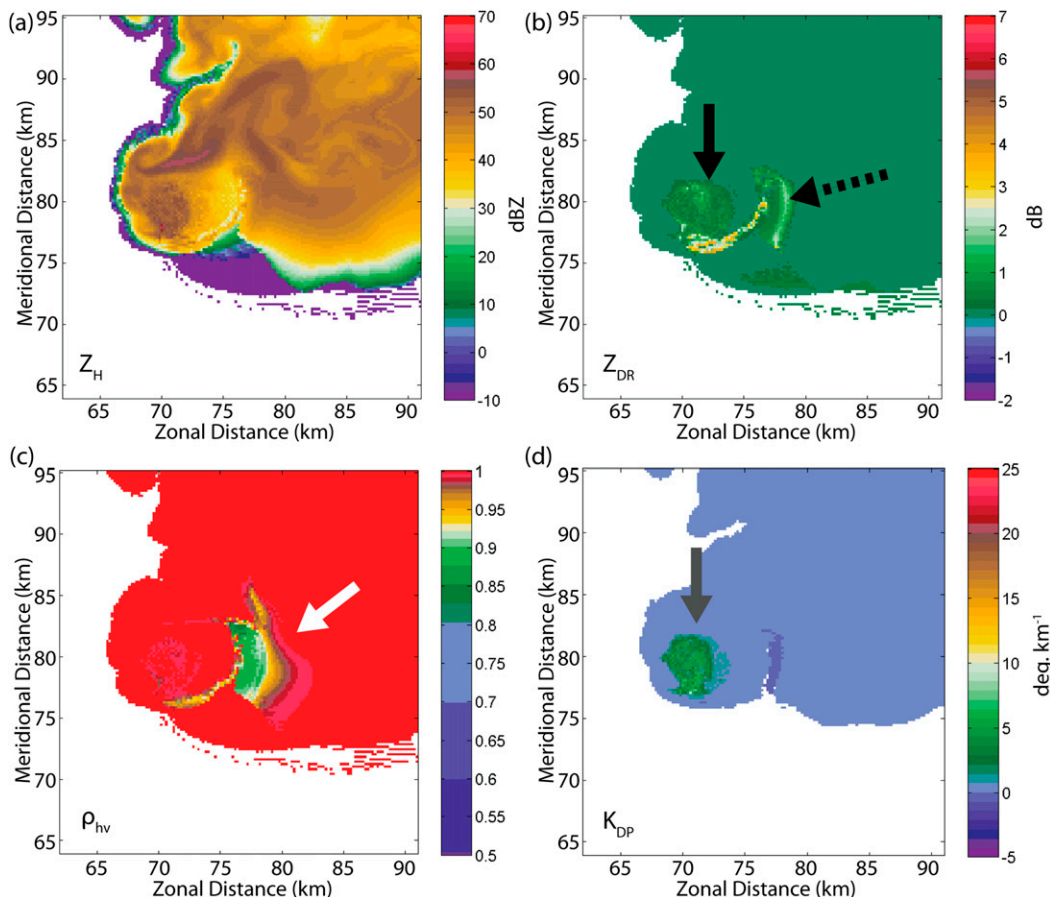
FIG. 2. Plots of (a) Z_H (dBZ), (b) Z_{DR} (dB), (c) ρ_{hv}, and (d) K_{DP} (° km^{-1}) at ~5400 m AGL from the 15q10 simulation valid at $t = 4800$ s at X band. In (b), a Z_{DR} half ring and a part of a Z_{DR} column are marked by a dotted and a solid black arrow, respectively. A ρ_{hv} half ring is identified by the white arrow in (c) and a dark-gray arrow identifies part of a K_{DP} column in (d).

Milbrandt and Yau (2005a), the gamma distribution can be written as

$$n_x(D) = N_{0x} D^{\alpha_x} \exp(-\lambda_x D),$$

where subscript x denotes a hydrometeor class (r for rain, g for graupel, h for hail, s for snow, i for ice crystals, and c for cloud water), D is particle equivolume diameter, N_{0x} is the concentration or intercept parameter, λ_x is the slope parameter, and α_x is a shape parameter.

The 0th, 3rd, and 6th moment of a gamma distribution are proportional to the total number concentration (N_{Tx}), hydrometeor mixing ratio (q_x), and radar reflectivity factor (z_x), respectively. Using this information, the mean mass diameter of rain, hail, and graupel (i.e., D_{mr}, D_{mh}, and D_{mg}, respectively) can be calculated. Derivations of relevant quantities, and representations of other distributions, are provided in Straka (2009).

The ability of a numerical model to produce realistic microphysical distributions depends, in part, on the number of moments predicted. Single-moment microphysics schemes (e.g., Kessler 1969; Lin et al. 1983) generally are the most basic in terms of capturing the effects of microphysical processes on size distributions. Multimoment schemes can simulate more complex PSDs by more completely modeling different microphysical processes (e.g., Ziegler 1985; Ferrier et al. 1995; Meyers et al. 1997; Reisner et al. 1998; Morrison et al. 2005; Milbrandt and Yau 2005a,b) and, thus, can result in more accurate depictions of hydrometeor distributions (e.g., Jung et al. 2012). For example, computing fall speeds weighted separately by multiple moments allows multimoment schemes to simulate sedimentation more accurately by providing a size sorting mechanism (e.g., Seifert and Beheng 2006; Milbrandt and Yau 2005a; Dawson et al. 2010, 2014) although not without potential issues when the shape parameter is fixed (Milbrandt and McTaggart-Cowan 2010). The triple-moment scheme presented in Milbrandt

TABLE 1. A summary of the relevant parameters used by the PRFO. The fractional water f_w of hail (h), graupel (g), and snow (s) is represented by f_{wh}, f_{wg}, and f_{ws}, respectively. Dry hail, dry graupel, and dry snow are represented by subscripts dh, dg, and ds, respectively. In the equations for the dielectric constant ε, $\varepsilon^{(a,b)}$ represents the dielectric constant, calculated using the Maxwell Garnett (1904) mixing formula, of a hydrometeor in which a is the matrix and b is the inclusion species. The PRFO does not include cloud water and ice crystals.

Parameter	Rain (r)	Hail (h)	Graupel (g)	Snow (s)
Aspect ratio (r_x)	r_r Brandes et al. (2002)	$r_{dg,dh} =$ Knight (1986) fit $$r_{g,h} = \begin{cases} f_{wg,wh}r_r + (1-f_{wg,wh})r_{dg,dh} & D_{wg,wh} < 9\,\text{mm} \\ f_{wg,wh}r_{r(9\text{mm})} + (1-f_{wg,wh})r_{dg,dh} & 9 \leq D_{wg,wh} \leq 20\,\text{mm} \\ 0.75 & D_{wg,wh} > 20\,\text{mm} \end{cases}$$		$r_s = 0.75 - f_{ws}(0.75 - r_r)$
Canting angle (°) mean ($\overline{\phi}_x$) and standard deviation (σ_x)	$\overline{\phi}_r = 0$ $\sigma_r = 0$	$\overline{\phi}_{g,h} = 0$ $\sigma_{g,h} = \begin{cases} 60 \times (1 - 2f_{wg,wh}) & f_{wg,wh} \leq 0.5 \\ 0 & f_{wg,wh} > 0.5 \end{cases}$		$\overline{\phi}_s = 0$ $\sigma_s = 20$
Dielectric constant (ε_x)	ε_r Cole and Cole (1941)	$\varepsilon_{wh} \approx \varepsilon^{(w,i)}$	$\varepsilon_{wg} \approx \varepsilon^{(w,s)} \approx \varepsilon^{[w(o,i)]}$	$\varepsilon_s \approx \varepsilon^{(o,i)}$ $\varepsilon_{w,s} = \frac{1}{2}[(1+\tau)\varepsilon^{(w,s)} + (1-\tau)\varepsilon^{(w,s)}]$ $\tau = \text{Erf}\left[\frac{2(1-f_{ws})}{f_{ws}} - 1\right]$
Density (ρ_x) (kg m^{-3})	$\rho_r = 1000$	$\rho_{dh} = 910$	$\rho_{dg} = 400$ $\rho_{wx} = \rho_{dx}(1-f_{wx}^2) + \rho_w f_{wx}^2$, where x is h, g, or s	$\rho_{ds} = 100$

and Yau (2005b; hereinafter MY3) predicts N_{Tx}, q_x, and z_x for all hydrometeors except cloud droplets (which are handled using two moments). Predicting the three moments lets one independently retrieve the three parameters of the gamma distribution, generally improves the depiction of size sorting relative to double-moment schemes (e.g., Milbrandt and Yau 2005a; Dawson et al. 2014), and can produce more realistic forecasts (e.g., Dawson et al. 2010, 2015, 2016). The MY3 scheme predicts six hydrometeor classes—rainwater ($\rho_r = 1000\,\text{kg m}^{-3}$), ice crystals ($\rho_i = 500\,\text{kg m}^{-3}$), snow ($\rho_s = 100\,\text{kg m}^{-3}$), hail ($\rho_h = 910\,\text{kg m}^{-3}$), graupel ($\rho_g = 400\,\text{kg m}^{-3}$), and cloud water ($\rho_c = 1000\,\text{kg m}^{-3}$). With the exception of ice, hydrometeor species in the MY3 scheme are spherical. Ice crystals are modeled as bullet rosettes.

b. PRFO

The framework for the PRFO used in this study is based upon that described by Jung et al. (2008, 2010) and Dawson et al. (2014). The PRFO calculates several common radar quantities, including equivalent radar reflectivity factor at horizontal (Z_H), differential reflectivity (Z_{DR}), specific differential phase (K_{DP}), and copolar correlation coefficient (ρ_{hv}). The reader is referred to available textbooks (e.g., Doviak and Zrnić 1993; Bringi and Chandrasekar 2001) and manuscripts (e.g., Zrnić and Ryzhkov 1999; Straka et al. 2000; Kumjian 2013a,b,c) for more details on these quantities.

The PRFO uses the distributions of rain, snow, graupel, and hail from MY3 to calculate relevant polarimetric fields. Pristine ice crystals and cloud water are not included in the PRFO because their contribution to the total radar return in severe convective storms is typically much smaller than that from hail, rain, graupel, and snow at common weather radar frequencies (e.g., below ~10 GHz). Details of the relevant characteristics of the PRFO are provided in Table 1.

Proper handling of mixed-phase hydrometeors such as wet hail is important when calculating polarimetric quantities. Unfortunately, this is not a straightforward task since most bulk schemes (including MY3) do not explicitly predict mixed-phased hydrometeors; the mass water fraction on a given frozen species x (f_{wx}) is not explicitly prognosed. Consequently, water fractions must be diagnosed separately. In the simulations presented herein, hail, snow, and graupel are assumed to be "wet" if they occur with rainwater at a given grid point; some (or all) of the rainwater mass is then redistributed onto the ice species to simulate mixed-phased hydrometeors following Dawson et al. (2014). This new diagnostic fractional water method allows the amount of water on hail and graupel to vary with the size of the particle as it works on discretized particle size ranges (e.g., bins) from the gamma PSDs; the diagnosed mass water fraction for a particle of a given size cannot exceed the critical water mass described in Rasmussen and

Heymsfield (1987). For example, whereas small hail can be associated with very high f_{wh} given sufficient amounts of rainwater, very large hail can only support limited f_{wh} since excess water is shed; rainwater that is not "reapportioned" onto ice that is present is kept as rain. This may end up removing too much rain (as in the case of a lot of hail and little rain), but since the microphysics scheme does not track liquid water fraction, it is difficult to know when rain and ice coexist as distinctly separate distributions and when they should be combined in some way to simulate water-coated ice (as in the case of melting hail or hail undergoing wet growth).

The method described in Dawson et al. (2014) and used in Johnson et al. (2016) has been developed to allow meltwater to soak graupel particles, increasing their density until it matches that of hail, after which point it is assumed that a water shell develops. Wet snow is handled essentially as in Jung et al. (2010) by comparing the amount of total snow mass with total rainwater mass—where rain and snow coexist, enough rain is moved into the snow category (equally for each size) that the resulting bulk fractional water for snow (f_{ws}) does not exceed 75%. In the figures and discussion of f_{wh}, f_{wg}, and f_{ws} in this paper, we will use a "bulk" mass water fraction, which is the mass-weighted mean water fraction integrated over the distribution.

The mean canting angle $\overline{\phi_x}$ is assumed to be 0° for all hydrometeors. The ratio of the minor to major axes (i.e., aspect ratio)[2] is important because polarimetric variables are often very sensitive to hydrometeor shape. Although the microphysics scheme assumes that rain, hail, graupel, and snow are spheres, we follow a more realistic approach in the PRFO by allowing aspect ratios to vary by hydrometeor size. The aspect ratio for rain decreases with increasing drop size (i.e., Brandes et al. 2002). Observations show that the shape of hail and graupel can vary (e.g., Macklin 1963; Browning 1966; Carte and Kidder 1966; Knight and Knight 1970a,b) according to size (e.g., Knight 1986; Giammanco et al. 2014) and water fraction (e.g., Browning and Beimers 1967). Here, the aspect ratios for hail and graupel vary linearly between that of a liquid raindrop of equivalent equivolume diameter and that given by a fit to the Oklahoma hailstones in Knight (1986) for particles less than ~9 mm. The

aspect ratios vary linearly between that of an ~9-mm raindrop and that of the Knight (1986) fit for particles between ~9 and 20 mm; they are fixed at 0.75 for particles larger than 20 mm (Table 1). The aspect ratio of snow varies between 0.75 if dry and that of an equivalent-sized raindrop if melted, not to be less than the aspect ratio of an ~9-mm raindrop. The practical effects of uncertainties and errors in the relationships between the aspect ratio, particle size, and fractional water are muted somewhat by the observation that those hydrometeors with arguably the most uncertainty in their size–aspect ratio relationship (e.g., hail, graupel, and snow) fall with varying canting angles (defined as the deviation of the minor or symmetry axis from vertical; e.g., hailstones may tumble or gyrate). A distribution of canting angles (denoted as σ_x—see Table 1) increases the "effective" aspect ratio toward unity and makes the hydrometeors appear more spherical/isotropic (thereby tending to reduce the magnitudes of Z_{DR} and K_{DP}).

The forward and backward scattering amplitudes of hydrometeors used in this study are calculated using the "transition matrix" (T matrix) code from Vivekanandan et al. (1991) as done in Jung et al. (2010); the values are calculated a priori, and a lookup table is used to speed calculations. The T-matrix code used for this project simulates mixed-phased hydrometeors as homogeneous mixtures of one species (i.e., the inclusion) embedded within a background species (i.e., the matrix); the Maxwell Garnett (1904) mixing formula is used for calculating the effective relative dielectric constant for mixed-phase hydrometeors. The calculated effective dielectric constant varies between that calculated using water inclusion with ice matrix and using ice inclusion with water matrix depending upon f_{ws} as in Ryzhkov et al. (2011).

Scattering amplitudes are calculated for particles with equivolume diameters of 0–8 mm split into 100 bins for rain, 0–20 mm split into 250 bins for graupel, 0–70 mm split into 875 bins for hail, and 0–30 mm split into 112 bins for snow. The resultant bin sizes are 0.08 mm for rain, hail, and graupel and 0.27 mm for snow. As implemented by Jung et al. (2010), the PRFO assumes that the elevation angle is always 0°. Since the largest impacts of canting angle variability tend to be for that component of canting angle that is projected onto the polarization plane, the PRFO used in this study assumes that canting occurs only in the polarization plane; a more complete treatment of two-dimensional canting as in Ryzhkov et al. (2011) will be implemented in future versions of the PRFO. Varying the elevation angle of the simulated radar data would add further complexity to the analyses since there would be additional

---

[2] There seem to be differing uses of the term "aspect ratio" (e.g., Ryzhkov et al. 2011) and "axis ratio" (Jung et al. 2010) to describe the shape of hydrometeors on orthogonal planes prescribed in forward operators. In this case, since the mean canting angle is 0° for all species, and the simulated radar elevation angle is also 0°, we use the terms interchangeably.

TABLE 2. Selected parameters used in all numerical simulations performed for this paper.

Model configuration	
Model	ARPS version 5.3.3 (Xue et al. 2000, 2001)
Horizontal grid spacing	Fixed—200 m
Vertical grid spacing	Stretched, ~85 m near the surface and ~375 m near model top
Domain size	$753 \times 753 \times 83$ ($150 \text{ km} \times 150 \text{ km} \times 20 \text{ km}$)
Time steps	Large: 1.0 s; small: 0.2 s
Computational mixing	Fourth order in horizontal and vertical
Microphysics	Three moments (N_T, q, z) for rain, hail, graupel, snow, and ice crystals; two moments (N_T, q) for cloud water (Milbrandt and Yau 2005a,b)
Turbulence parameterization	Anisotropic 1.5-order turbulent kinetic energy (TKE)
Boundary conditions	Lateral: radiation; bottom: rigid, free-slip; top: rigid, Rayleigh damping
Initial perturbation	Magnitude: 4 K; shape: $10 \text{ km} \times 10 \text{ km} \times 1.5 \text{ km}$; elliptical bubble centered 1.5 km AGL

dependencies on the location of the radar relative to the simulated convective storm and on the specific elevation angle assumed.

In general, attenuation by rain at X band can be an order of magnitude greater than that at S band (e.g., Bringi et al. 1990; Park et al. 2005a; Snyder et al. 2010), although the behavior of attenuation in (wet) hail as a function of radar wavelength is more complicated (e.g., Aydin and Zhao 1990; Vivekanandan et al. 1990; Borowska et al. 2011; Ryzhkov et al. 2013a,b). The effects of attenuation, however, are not included in the simulations presented in this paper primarily for two reasons. First, attenuation at X band can be estimated and its effects removed or reduced; the quantitative use of X-band radar data often requires attenuation correction, anyway. Second, since the appearance of precipitation sampled by an X-band radar depends upon the cumulative effects of attenuation, including attenuation herein would greatly add to the complexity of analyses since some of the radar fields would change substantially depending upon the "viewing angle" of the radar relative to the simulated supercells. So as not to expand further the dimensionality of the parameter space, the effects of attenuation will not be included in the results presented herein; when comparing with real X-band data, attenuation-corrected observations will be shown.

c. Numerical simulations

Since supercells occur in a wide range of environments, we have performed eight different simulations using different background wind profiles; varying the wind profiles in the different simulations provides us with more robust aggregate statistics by expanding the sample size beyond just one or two simulations. Where necessary, substantial similarities or differences in the results as a function of wind profile characteristics will be noted, but this work is not intended to intensively focus on the specific role of different wind

profiles on the polarimetric structure of the simulated supercells.

Version 5.3.3 of the Advanced Regional Prediction System (ARPS; Xue et al. 2000, 2001, 2003) is used for this study. Simulations are performed on a $151 \text{ km} \times 151 \text{ km} \times 20 \text{ km}$ grid. The horizontal grid spacing of 200 m was chosen as a compromise between computational efficiency and the desire to resolve as much detail of relevant storm-scale [$\sim O(1 \text{ km})$] structures as possible (e.g., Bryan et al. 2003; Petch 2006). The initial updraft is developed from an ellipsoidal warm bubble [à la Klemp and Wilhelmson (1978) and many others]. The grid for each simulation is translated so as to keep the primary convective cell as near as possible to the center of the domain, although this was not always possible since grid translation was fixed while storm motion was sometimes unsteady. Model fields are saved every 120 s, and each simulation is run for 10 800 s. Several simulations develop unrealistically strong low-level inflow toward the end of the simulation period resulting from boundary issues that arise when the updraft approaches a lateral boundary. Additionally, many simulations produce more widespread convection near the location of the primary cyclonic supercell after ~9000 s, which leads to increasing storm interactions. To minimize the impact these have on the analyses, this study focuses primarily on the 1800–9000-s period. A summary of the model configuration can be found in Table 2. The thermodynamic sounding for all simulations (Fig. 3a) is based on the analytic sounding of Weisman and Klemp (1982, hereinafter WK82) with sufficient convective available potential energy (CAPE; $\sim 2000 \text{ J kg}^{-1}$) to support severe convective storms.

Changes in supercell organization and intensity resulting from differences in the background flow field (e.g., WK82; Weisman and Klemp 1984; Rotunno and Klemp 1982, 1985; Rasmussen and Blanchard 1998; Rasmussen 2003; Thompson et al. 2003; Craven and Brooks 2004) are likely to be associated with corresponding changes in the
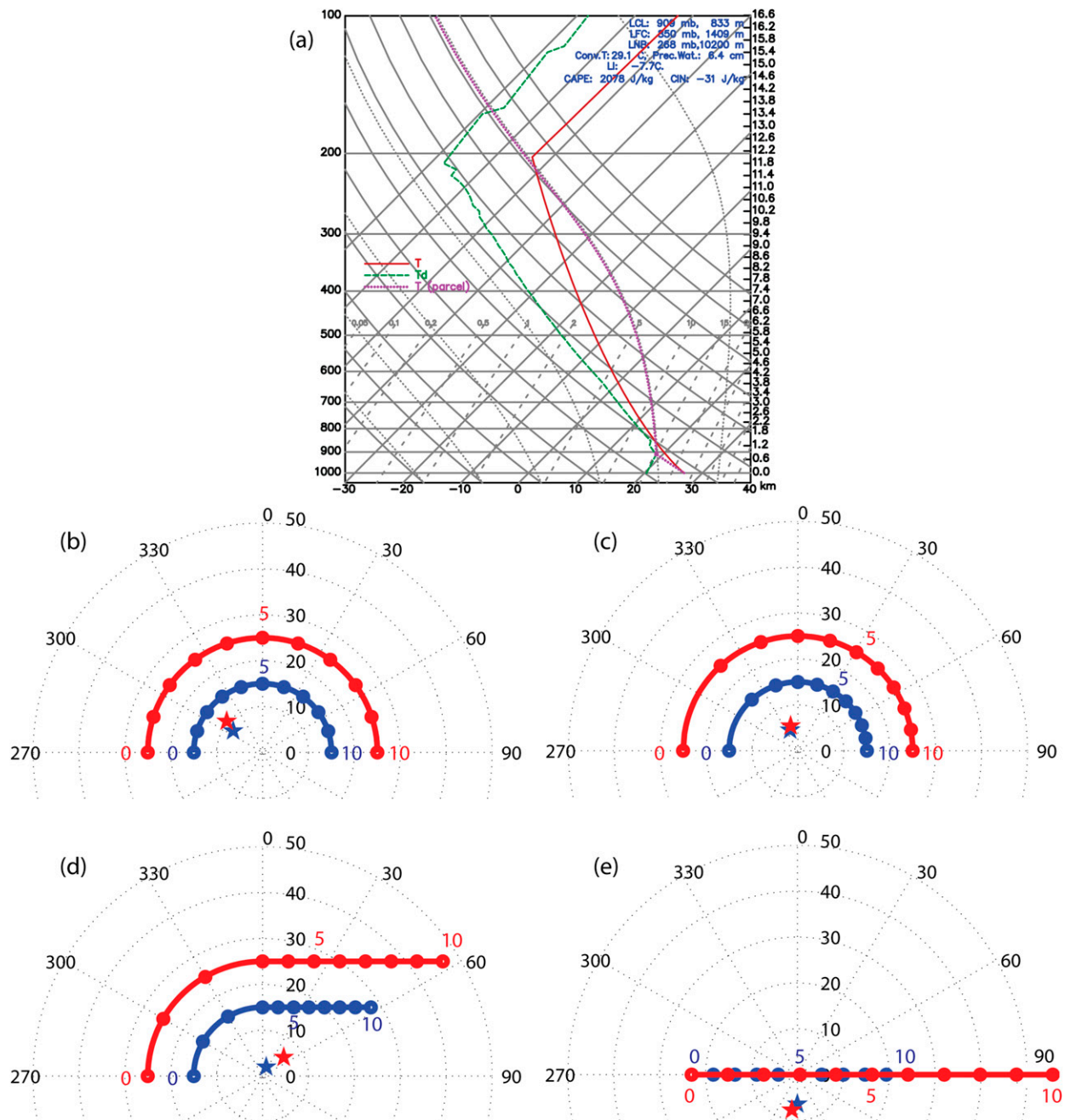
FIG. 3. (a) A skew-*T*, log-*P* plot of the idealized sounding used for the eight primary simulations examined in this study. The sounding is based on the analytical sounding presented in Weisman and Klemp (1982); the long and short dashed lines highlight the environmental and surface parcel freezing (0°C) levels, respectively. The four hodograph shapes examined in this study: (b) half circle with constant veering between the surface and 10 km AGL (15r10 and 25r10), (c) half circle with decreasing shear and veering between the surface and 10 km AGL (15r10_057 and 25r10_057), (d) quarter circle with 90° of turning from the surface to 3 km AGL with constant, ''straight'' shear from 3 to 10 km AGL (15q10 and 25q10), and (e) straight-line hodograph with constant shear between the surface and 10 km AGL (15str and 25str). The blue curves represent the weak shear cases (mean 0–10-km shear ~ 4.7 × 10⁻³ s⁻¹); the red curves represent the strong shear cases (mean 0–10-km shear ~ 7.9 × 10⁻³ s⁻¹). All hodographs of the same color are the same length. Sounding heights are marked every 1 km by circles along each hodograph, with the 0-, 5-, and 10-km heights marked in numbers. Red and blue stars in each panel represent an estimated storm motion based on peak updraft motion between 4800 and 8400 s. The wind speeds (labeled from 0 to 50) are in meters per second, and winds above 10 km are constant.

polarimetric signatures, but this has been largely unexplored in the context of polarimetric signatures in idealized numerical simulations. In this study, eight idealized simulations are performed that differ only in the initial vertical wind profile. Note that the primary reason for using different wind profiles is to increase the sample size for the analysis of the signatures, although some relevant differences in the radar fields as a function of wind profile will be pointed out where appropriate. These different vertical wind profiles have been created by systematically modifying the shape, length, and "distribution" of the shear; the hodographs, to varying extents, have been found to support severe convective storms and supercells (e.g., Brooks and Wilhelmson 1993). The eight hodographs used in this study are designed as follows (Figs. 3b–e):

- We use two half-circle hodographs of radius $S = 15 \, \text{m s}^{-1}$ and $S = 25 \, \text{m s}^{-1}$ with constant veering of winds between the surface and 10 km AGL; the wind direction changes 180° at a constant rate in the 0–10-km layer. These simulations are referred to as experiments 15r10 and 25r10.
- We use two half-circle hodographs of radius $S = 15 \, \text{m s}^{-1}$ and $S = 25 \, \text{m s}^{-1}$ with wind shear maximized near the surface and decreasing to a height of 10 km; the wind direction changes 90° in the 0–3-km layer and another 90° in the 3–10-km layer (i.e., the wind veers exponentially less with increasing height). These simulations are referred to as experiments 15r10_057[3] and 25r10_057.
- We use two hodographs characterized by a quarter-circle shape with radius $S = 15 \, \text{m s}^{-1}$ and $S = 25 \, \text{m s}^{-1}$ in the 0–3-km AGL layer with constant shear on a straight-line hodograph from 3 to 10 km AGL. These simulations are referred to as experiments 15q10 and 25q10.
- We use two straight-line hodographs with constant shear (along a straight hodograph) between 0 and 10 km. These simulations are referred to as experiments 15str and 25str.

In all environments, there is no wind shear above 10 km. The lengths of the "weak" shear hodographs (i.e., 15r10, 15r10_057, 15q10, and 15str) are the same with 0–10-km layer mean shear of $4.7 \times 10^{-3} \, \text{s}^{-1}$; the lengths of all "strong" shear hodographs (i.e., 25r10, 25r10_057, 25q10, and 25str) are the same with 0–10-km mean shear of $7.9 \times 10^{-3} \, \text{s}^{-1}$.

----

[3] The "_057" comes from the exponent used in the equations for the u and v components of the horizontal wind: $u(z) = S \times \cos[\pi(1 - z^{0.5757}/10\,000)]$ and $v(z) = S \times \sin[\pi(1 - z^{0.5757}/10\,000)]$.

3. Simulated ρ_{hv} rings

Resonance effects associated with scattering by hailstones can result in large differences between X-band and S-band polarimetric fields (e.g., Figs. 1–2). Simulations performed herein produce polarimetric radar fields in hail-bearing regions that are consistent with observations. For example, Fig. 4 shows Z_H, Z_{DR}, ρ_{hv}, and K_{DP} at S band and X band from one time in the 25r10_057 simulation; several relevant microphysical fields are shown in Fig. 5. Where q_h exceeds approximately $1 \, \text{g kg}^{-1}$ (Fig. 5b) and D_{mh} exceeds ~10 mm (Fig. 5d) in region of the forward-flank hail signature (e.g., KR08), Z_H at S band is generally 5–10 dBZ greater than it is at X band. In these same areas, Z_{DR} is ~(1.5–2) dB at S band but is generally greater than 2.5 dB at X band. In addition, ρ_{hv} at X band drops below 0.90 (and even below 0.7 near the tip of the hook echo where D_{mh} exceeds 40 mm), whereas it is generally greater than 0.90 at S band. The relationship between K_{DP} at S band and that at X band is less consistent in areas with $q_h > 1 \, \text{g kg}^{-1}$, but the ratio of X-band to S-band K_{DP} in areas of rain is as expected based upon the wavelength difference. In addition, a feature resembling a Z_{DR} arc (e.g., KR08; Dawson et al. 2014) is also evident in both $D_{m,h}$ and Z_{DR}. Again, in general, the differences observed in the radar fields at X band versus those at S band in areas with nonnegligible amounts of hail (e.g., $q_h > 1 \, \text{g kg}^{-1}$) agree with the observations presented earlier.

a. Kinematic and microphysical composition

A band of reduced ρ_{hv} thought to encircle, partially or completely, the periphery of a supercell's updraft has been observed in previous studies (e.g., KR08; Payne et al. 2010; Snyder et al. 2013). The so-called ρ_{hv} ring is seen as a ring or half ring along the eastern (downshear) periphery of the updraft. Throughout this section, no distinction will be made between a half ring and a full ring; the feature will be referred to simply as a "ρ_{hv} ring." In addition, unless otherwise explicitly stated, all references to radar quantities in this section pertain to those calculated at X band.

All simulations that were part of this study produced ρ_{hv} rings associated with the primary cyclonic supercell, although the simulations with straight hodographs (i.e., 15str and 25str) produced much less prominent ρ_{hv} rings than the other simulations. A representative example of a ρ_{hv} ring as seen at a height above the environmental 0°C level but below the updraft-perturbed 0°C level is shown from the 25r10 simulation in Fig. 6. In this case, the ρ_{hv} ring is nearly a complete ring located along the periphery of the updraft where vertical velocity w is
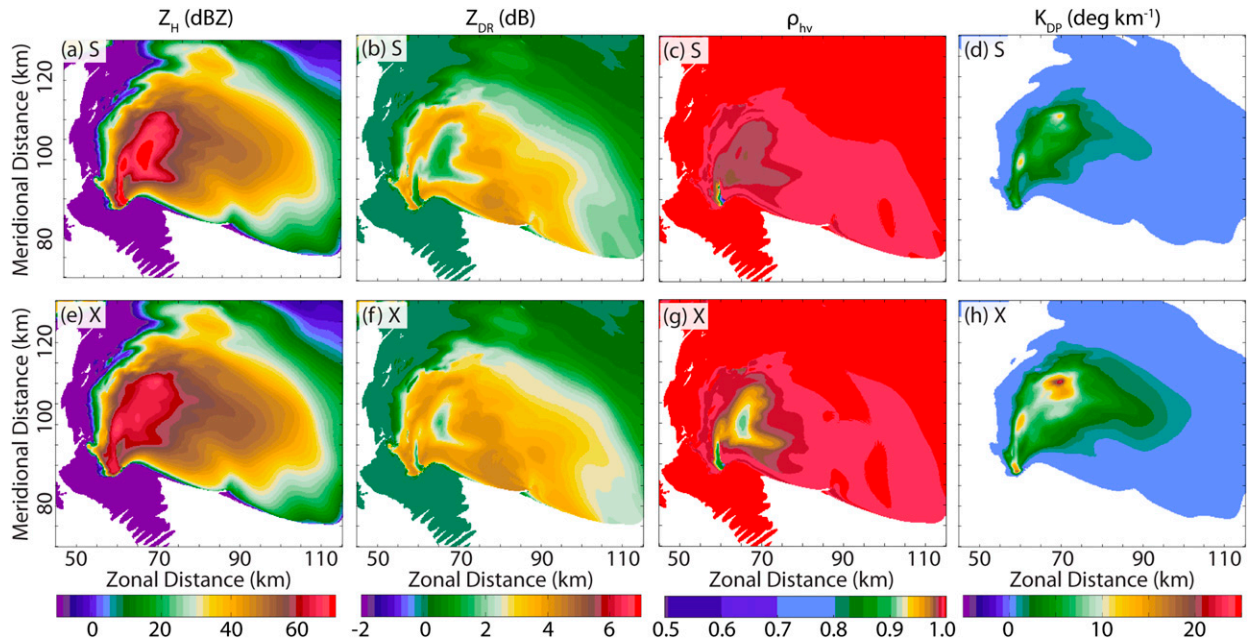
FIG. 4. Polarimetric fields from the 25r10_057 simulation at (top) S and (bottom) X bands for (left) Z_H (dBZ), (left center) Z_{DR} (dB), (right center) ρ_{hv}, and (right) K_{DP} (° km^{-1}). The area of low Z_{DR} and relatively low ρ_{hv} at S band is caused by hail (see q_h, Fig. 5, below) with relatively high f_{wh}, which, apparently, is masking the low-level hail signature at X band. Data are valid at a height of 120 m.

generally 10–30 m s^{-1} (Fig. 6a). Some evidence of a weak echo region is seen in the eastern half of the updraft, and the ρ_{hv} ring is nearly collocated with a Z_{DR} ring (Fig. 6b). The eastern side of the ρ_{hv} ring is characterized by a relatively small amount ($q_h < 0.5$ g kg^{-1}) of moderately sized ($D_{mh} \sim 5$–13 mm), wet ($f_{wh} \sim 20\%$–60%) hail (Figs. 6c,d); graupel in this area is drier and even more limited in amount and size (Figs. 6e,f). The western side of the ρ_{hv} ring is similar except that there is more hail (i.e., $q_h > 2.5$ g kg^{-1}) and graupel ($q_g > 2$ g kg^{-1}). On the far northern periphery of the updraft, there is another local minimum in ρ_{hv} that is the result of moderately sized ($D_{mh} \sim 7$–10 mm), dry hail.

Some of these characterizations are seen in observations of a supercell that occurred in central Oklahoma in 2013 and was sampled by RaXPol (Pazmany et al. 2013). Unfortunately, the radar was quite close to the storm and did not scan at a sufficiently high elevation angle to sample above ~5 km AGL; an ongoing intense tornado drew the attention of the radar operators at this time. The quantities Z_H, Z_{DR}, K_{DP}, and ρ_{hv} on a ~4.0 km AGL constant-altitude plan position indicator (CAPPI) are shown in Fig. 7. A zone of reduced ρ_{hv} akin to a ρ_{hv} ring is apparent to the immediate exterior of an area of enhanced Z_{DR} that is marked by the solid white curve in all panels. Differences between the east and west sections of this ρ_{hv} ring are akin to those associated with the simulated ρ_{hv} ring shown in Fig. 6. For example, the

eastern part of this ρ_{hv} ring is generally characterized by, relative to the western part, lower Z_H (i.e., 30–40 dBZ vs 40–50 dBZ) and lower K_{DP} (i.e., 0°–1° km^{-1} vs 1°–4° km^{-1}). The Z_{DR} in most of this observed ρ_{hv} ring is near 0 dB, which is dissimilar to the one example shown in Fig. 6. However, ρ_{hv} is still reduced (i.e., 0.9–0.4) within primarily the northern and western region of enhanced Z_{DR} and K_{DP} (i.e., within the solid white curve). Of course, the simulation in Fig. 6 and observations in Fig. 7 are different storms in different environments, so it is difficult to know how much of the differences is the result of differences in environmental characteristics and storm structure as compared with those caused by legitimate discrepancies between the model/microphysics/PRFO and the natural world.

In contrast to the analysis at ~4600 m AGL shown in Fig. 6, the ρ_{hv} ring above the updraft-perturbed 0°C level (i.e., ~5600 m AGL as in Fig. 8) is only seen along the eastern and northeastern periphery of the updraft near the gradient between the updraft and downdraft. The area of reduced ρ_{hv} and the magnitude of the minimum ρ_{hv} are strongly associated with D_{mh} such that the lowest ρ_{hv} is found in the area of largest D_{mh}. Within the ρ_{hv} ring, q_r, q_h, and q_g are relatively low (i.e., <1 g kg^{-1}). The ρ_{hv} ring is immediately east (i.e., downshear) of an arcing area of reduced Z_H that represents the weak echo region. The bulk (i.e., mass-weighted mean integrated over the distribution) water fraction of hail ranges from ~30% on
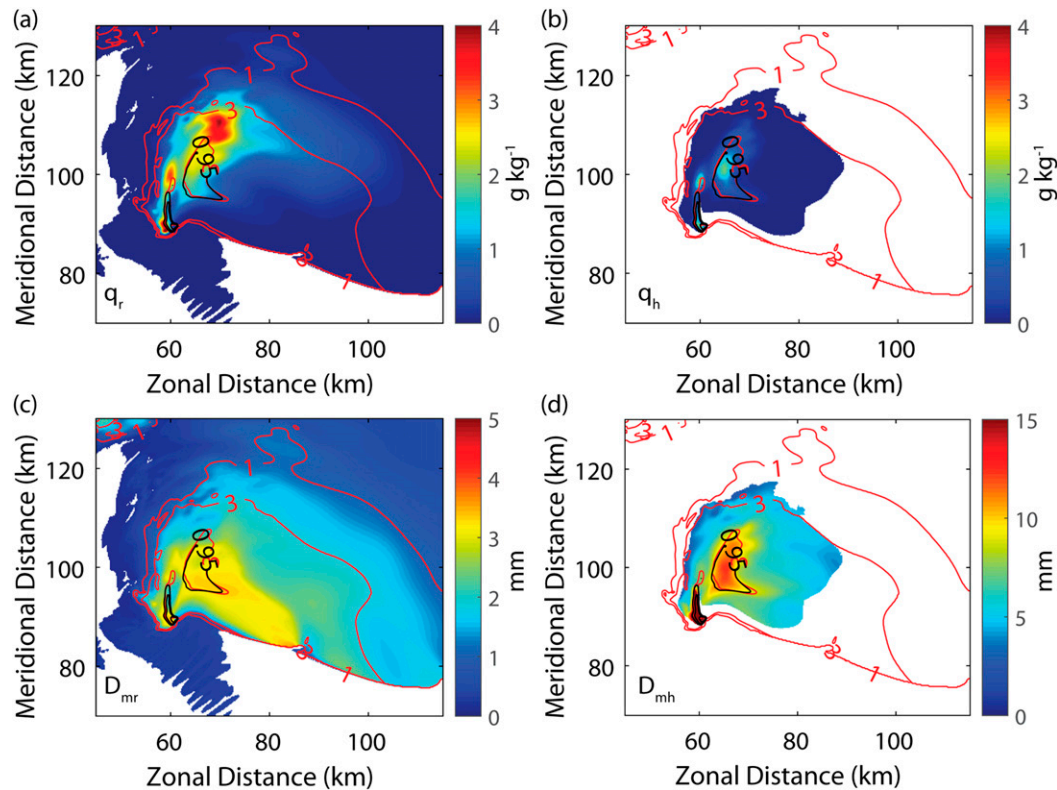
FIG. 5. Plots of (a) q_r (g kg^{-1}), (b) q_h (g kg^{-1}), (c) D_{mr} (mm), and (d) D_{mh} (mm) valid at the same time for the same simulation as Fig. 4. In (a)–(d), the X-band Z_{DR} of 1 and 3 dB is contoured in red and X-band ρ_{hv} of 0.95 is contoured in black.

the southern end to <5% on the northern end; there is very little graupel present at this level within the ρ_{hv} ring, but what little is there is wet (e.g., f_{wg} of 20%–70%).

In general, a similar evolution of the ρ_{hv} ring with height is seen in the other simulations as well. A pseudo-volumetric perspective of the ρ_{hv} ring from the 25q10 simulation details the structure of the ρ_{hv} ring (Fig. 9). As viewed from the top looking downward, several areas of $\rho_{hv} < 0.95$ can be seen—an arcing band on the east side of the updraft, a quasi-circular area north of the updraft, and an oval area to the west of the updraft. When viewed from the west looking toward the east, it is apparent that the first area noted above is the ρ_{hv} ring that extends to altitudes above the updraft-perturbed 0°C level, and the ring tilts downward along the northeastern periphery of the updraft. The short (<2 km AGL), quasi-circular zone of reduced ρ_{hv} is essentially connected to the ρ_{hv} ring; the area of reduced ρ_{hv} to the west of the updraft is only primarily evident only within several kilometers of the ground. All areas of reduced ρ_{hv} are associated with local maxima in hail size, with the largest hail near the ground occurring along the southwest side of the storm (near the inside part of the hook

echo). For as yet unknown reasons, this location is commonly found to have the largest D_{mh} in the simulations performed in this study.

To further illustrate this, we show a south-to-north vertical cross section through the updraft in the 25r10 simulation at 7320 s (Fig. 10) and point out three areas of reduced ρ_{hv}. The first area of lowered ρ_{hv} is along the north side of the updraft (e.g., 75–80 km along the abscissa) below ~5700 m AGL and is associated with $D_{mh} \sim 12$–15 mm and $f_{wh} \sim 20\%$–40%; this local maximum in hail size appears to be the result of size sorting within the updraft (color shaded in Fig. 10d). The values of ρ_{hv} associated with this hail are lower at X band (i.e., 0.91–0.95) than they are at S band (i.e., 0.94–0.97), implying yet again that ρ_{hv} at X band may be more useful than it is at S band for detecting large (wet) hail, at least as long as signal quality is sufficient (e.g., the signal is not very severely attenuated such that low signal-to-noise results in ρ_{hv} biases) and other radar artifacts are not detrimentally and disproportionately affecting the X-band radar. The second area of reduced ρ_{hv} is found near the top of the Z_{DR} column between 4500 and 5600 m AGL, where large amounts of rain and very wet hail ($f_{wh} > 80\%$) and
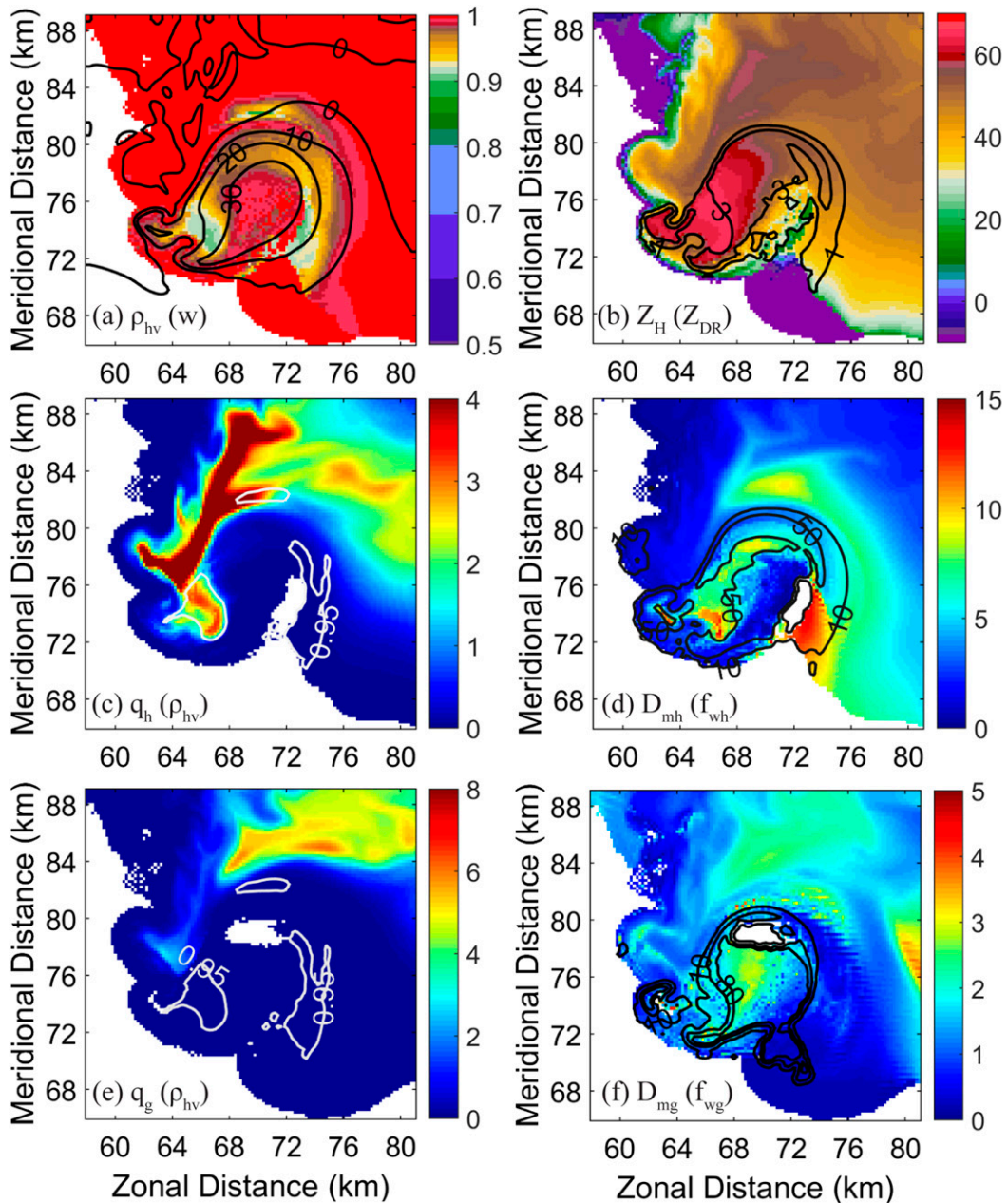
FIG. 6. A well-defined ρ_{hv} ring in the 25r10 simulation at $t = 7320$ s and ~4600 m AGL, as shown by (a) ρ_{hv} (colors) and w (contoured every 10 m s^{-1}), (b) Z_H (dBZ; colors) and Z_{DR} (dB; contoured every 1 dB), (c) q_h (g kg^{-1}; colors) and ρ_{hv} (contoured at 0.95), (d) D_{mh} (mm; colors) and bulk f_{wh} (contoured every 20%), (e) q_g (g kg^{-1}; colors) and ρ_{hv} (contoured at 0.95), (f) D_{mg} (mm; colors) and bulk f_{wg} (contoured every 20%). All radar quantities are calculated at X band.

graupel exist. The third area of interest (at 81–82 km along the abscissa) is characterized by a narrow column of ρ_{hv} that decreases from ~0.97 near 7 km AGL to ~0.86 near 2 km AGL and is only apparent at X band; S-band ρ_{hv} in this area is 0.990–0.995. This column of lowered ρ_{hv} is associated with a vertically oriented zone of locally larger hail ($D_{mh} \sim 7$–10 mm). When looking at all simulations,

ρ_{hv} at X band is generally lower than it is at S band where mixed-phased hydrometeors are present, particularly in areas of large, wet hail. The area of reduced ρ_{hv} at X band above the 0°C level near the 80–82-km area along the abscissa is along the eastern periphery of the updraft and is associated with a local maximum in D_{mh}, low but non-zero q_r, and q_h of generally 4–10 g kg^{-1}.
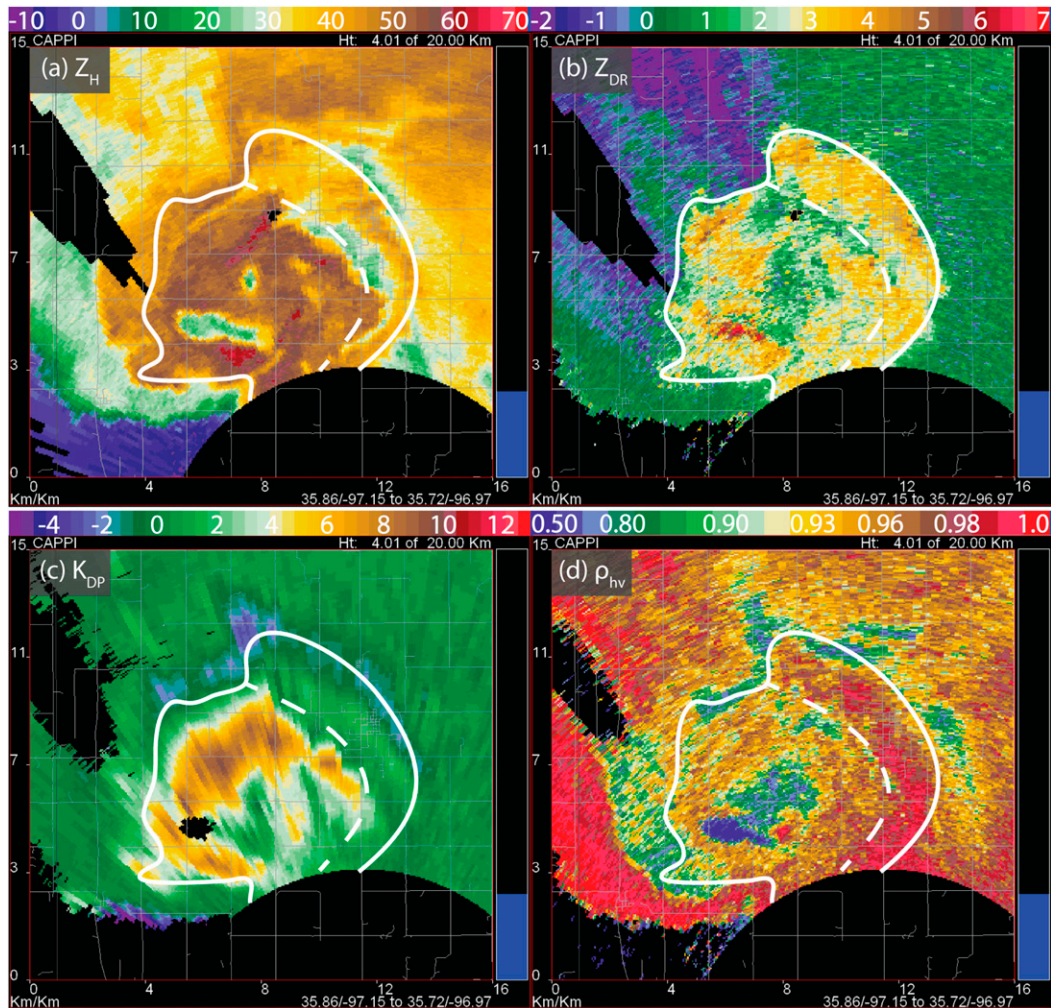
FIG. 7. CAPPI data collected by RaXPol as a supercell was producing a significant tornado northeast of Oklahoma City, Oklahoma, on 19 May 2013: (a) Z_H (dBZ), (b) Z_{DR} (dB), (c) K_{DP} (° km^{-1}), and (d) ρ_{hv} data, valid at ~4.0 km above radar level, which is approximately the height of the environmental 0°C level as sampled by an 1800 UTC sounding launched from Norman, Oklahoma. The white outline marks the approximate edge of Z_{DR} > 2 dB; the white dashed curve separates two regions of the area of enhanced Z_{DR} that have distinctly difference polarimetric characteristics.

The magnitude of ρ_{hv} above the 0°C height within ρ_{hv} rings observed at X band as reported in Snyder et al. (2013) sometimes dropped below 0.50, which is less than that associated with previously published ρ_{hv} rings at S band (e.g., KR08; Payne et al. 2010; Picca and Ryzhkov 2012). The simulations support the observation that ρ_{hv} at X band tends to be less than that at S band, although the minimum ρ_{hv} in these simulations (~0.80) does not get as low as that observed in Snyder et al. (2013). For example, from the 25q10 simulation, the minimum value of ρ_{hv} along the eastern periphery of the updraft at 4080 s and ~5600 m AGL is 0.95 and 0.88 at S and X bands, respectively (Fig. 11). We suspect that the simulated ρ_{hv} is not as low as seen in some observations because we

assume hailstones are oblate spheroids with a prescribed density, aspect ratio, and canting angle variability; the diversity of hailstone shapes, densities, and dielectric properties is likely much more complex in nature than what we can prescribe at this time. Regardless, it is quite apparent that not only is ρ_{hv} within the ring lower at X band than it is at S band, the ρ_{hv} ring is also considerably larger at X band.

b. Bulk correlations

The ρ_{hv} rings observed in the weak shear simulations tend to be less steady than those observed in the strong shear simulations. In general, the weak shear simulations tended to produce ρ_{hv} rings that were considerably
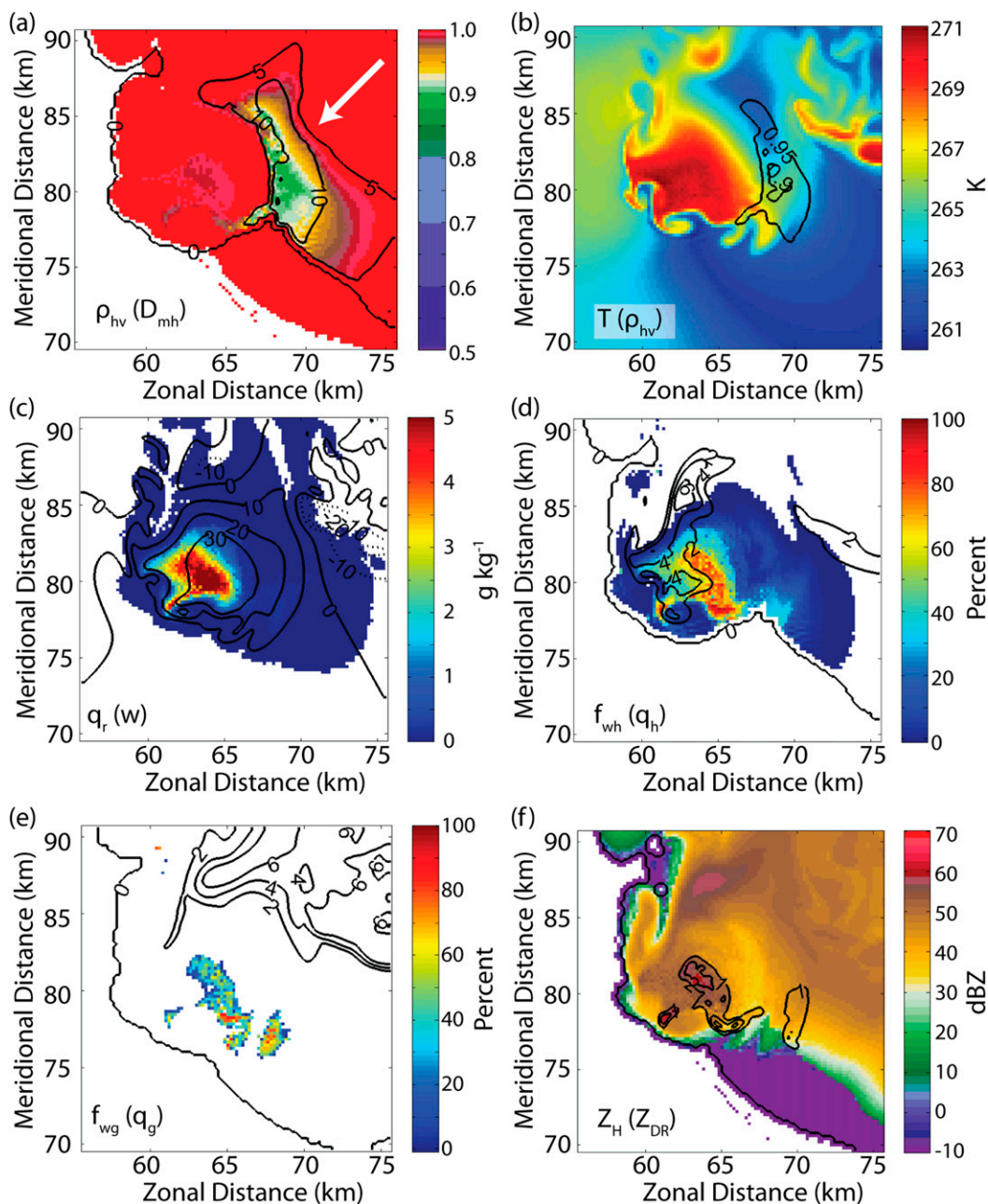
FIG. 8. A ρ_{hv} ring in the 25r10 simulation at $t = 4800\,s$ and $\sim 5600\,m$ AGL, as shown by (a) ρ_{hv} (colors) and D_{mh} (contoured every 5 mm), (b) T (colors; K) and ρ_{hv} (contoured at 0.95), (c) q_r (colors; g kg^{-1}) and w (contoured every 10 m s^{-1}), (d) f_{wh} (colors) and q_h (contoured every 2 g kg^{-1}), (e) f_{wg} (colors) and q_g (contoured every 2 g kg^{-1}), and (f) Z_H (colors; dBZ) and Z_{DR} (contoured every 1 dB). All radar quantities are calculated at X band. All contoured data have been filtered by a 3×3 (i.e., 600 m $\times$ 600 m) averaging filter to enhance clarity. The white arrow in (a) points to the ρ_{hv} ring. As a reminder, the bulk f_{wg} and f_{wh} values shown are mass-weight mean values over the distribution.

smaller and had weaker minima than those produced in the strong shear simulations (e.g., as quantified as the area in which $\rho_{hv} < 0.95$). There were two exceptions to this. First, the 25str simulation, like the 15str simulation, only produced very intermittent, ill-defined, and weak

ρ_{hv} rings east of the updraft through much of the first $\sim 7000\,s$ of the simulation. The two simulations that used a straight-line hodograph tended to have weaker storm-relative winds directed toward the updraft in the 4–6-km layer where the ρ_{hv} rings in the other simulations
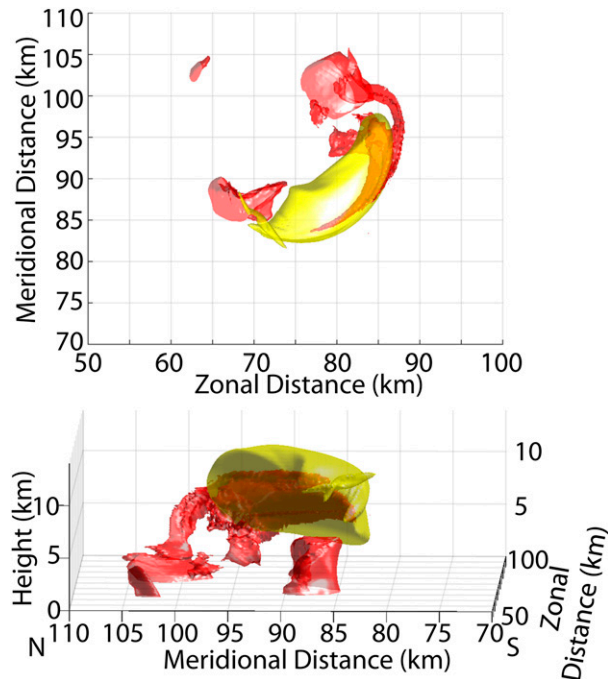
FIG. 9. Isosurfaces of $\rho_{\rm hv} = 0.95$ (red) and $w = 30\,{\rm m\,s}^{-1}$ (yellow) valid 6000 s from the 25q10 simulation looking (top) directly downward and (bottom) nearly due eastward from west of the supercell.

were most often found. In addition, 15str and 25str tended to have smaller hail (and smaller areas of moderate and large hail) aloft; a more complete hydrometeor trajectory analysis would be required to assess whether the flow within and near the updraft was unfavorable for the development of larger hail. The second exception to the general weak shear–small $\rho_{\rm hv}$ rings/ strong shear–large $\rho_{\rm hv}$ rings relation was the 15q10 simulation, which produced particularly robust and large $\rho_{\rm hv}$ rings relative to the other weak shear cases. Relative to the other weak shear simulations, the 15q10 simulation tended to have stronger storm-relative, midlevel winds, particularly in the component directed toward the updraft on the downshear side of the updraft. The 15r10, 15r10_057, 15str, and 15q10 simulations had $\rho_{\rm hv}$ rings that averaged 0.45, 0.92, 0.18, and 11.89 km^2 in horizontal extent at $\sim$5350 m AGL; $\rho_{\rm hv}$ rings in the 25r10, 25r10_057, 25str, and 25q10 averaged 6.71, 12.95, 0.04, and 17.2 km^2. The largest $\rho_{\rm hv}$ rings, at least at $\sim$5350 m AGL, were produced by the 15q10, 15r10_057, and 25q10 simulations. The smallest $\rho_{\rm hv}$ rings occurred in the 15str and 25str simulations

The areal extent of the $\rho_{\rm hv}$ rings at a given altitude was, in general, well correlated with the areal extent of hail at that altitude. For example, the trends between the area of $\rho_{\rm hv} < 0.95$ and the area of $D_{mh} > 5$ mm at

$\sim$5350 m AGL in the 15q10 and 25r10 simulations are very similar (Fig. 12); values of the (linear) Pearson correlation coefficient (hereinafter r) between the size of the $\rho_{\rm hv}$ ring and the spatial extent of $D_{mh} > 5$ mm in this simulation are 0.78 and 0.91 at S and X bands, respectively. As can be inferred in Fig. 13, the minimum value of $\rho_{\rm hv}$ at $\sim$5350 m AGL from all simulations was strongly negatively correlated (i.e., $r < -0.5$) with the maximum value of D_{mh}, the area of $D_{mh} > 5$ mm, and the areal extent of the $\rho_{\rm hv}$ ring at 5350 m. The size of the $\rho_{\rm hv}$ ring was positively correlated with maximum updraft intensity, the horizontal area where $D_{mh} > 5$ mm, and the maximum D_{mh} at 5650 m AGL.

4. Conclusions

To study the microphysical structure of several commonly observed polarimetric signatures within supercells, we performed eight high-resolution simulations using the MY3 scheme and a PRFO. To increase the sample size and better establish relationships between the signatures and the microphysical and kinematic structure of simulated supercells, eight simulations were carried out using eight hodographs of four "shapes" and two lengths. These simulations still yielded a small sample size, but the decision to modify only the vertical shear profile was made to limit the parameter space and degrees of freedom while still allowing us to look at supercells in a variety of different environments with hodographs commonly associated with convective storms and supercells. Given current thoughts and evidence of the effect of vertical wind shear on supercell morphology and evolution, we should expect there to be repeatable and systematic changes in the polarimetric structure as shear changes; it is difficult to identify systematic changes, though, without a large sample size, robust microphysics, and an advanced PRFO.

Past research has focused on the structure of microphysical parameters within simulated supercells, but there has been comparatively little examination of simulated polarimetric signatures in three-dimensional, high-resolution supercell simulations. A PRFO can be a valuable tool for examining how well bulk microphysics schemes capture microphysical distributions and processes occurring within convective storms by allowing for more direct comparisons with radar observations. In the two parts of this paper, we aimed to examine if the MY3 scheme used in a high-resolution numerical model can reproduce several commonly seen polarimetric signatures. The appearance of the signatures examined in this paper—specifically, $\rho_{\rm hv}$ rings and, as shown in Part II, $Z_{\rm DR}$ and $K_{\rm DP}$ columns—were examined primarily at X band, though notable differences were highlighted
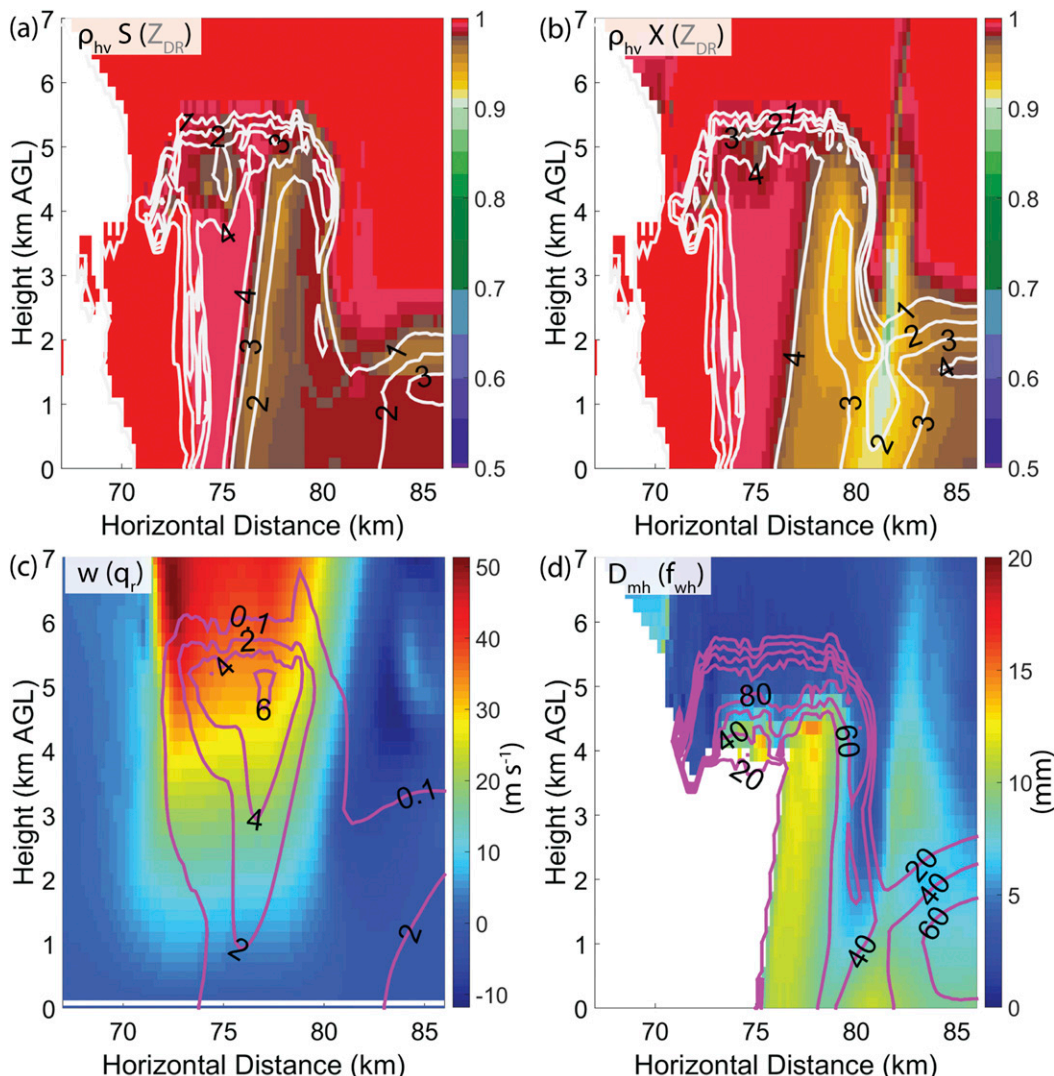
FIG. 10. A south-to-north vertical cross section of ρ_{hv} (colors) and Z_{DR} (contoured every 1 dB) at (a) S band and (b) X band, (c) w (colors) and q_r (contoured every 2 g kg^{-1}), and (d) D_{mh} (colors; mm) and f_{wh} (contoured every 20%). Data are from the 25r10 simulation at 7320 s.

where particular sensitivities to radar wavelength appeared.

We now revisit the three main foci, at least as they pertain to ρ_{hv} rings, outlined at the beginning of this paper. Many of the simulations do indeed produce structures that look like ρ_{hv} rings; these rings were larger in size and had lower ρ_{hv} minima at X band than they did at S band. Particularly evident in the 15q10, 25q10, 25r10_057, and 25r10 simulations, the rings generally became less "complete" with increasing height above the environmental 0°C level. They tended to be found on the west, north, and east sides of the updraft at altitudes of 4500–5000 m AGL but only on the southeast through northeast sides of the updraft at higher altitudes. At

lower heights, q_r, q_h, and q_g were largest in the western part of the ρ_{hv} rings where a wet hail and rain mixture seemingly contributed to the reduction in ρ_{hv}, whereas they were all more limited in the eastern sections and at higher altitudes (e.g., near and above the updraft-perturbed 0°C level). The simulated ρ_{hv} rings were highly correlated with, among other quantities, the area of $D_{mh} > 5$ mm aloft, and the magnitude of ρ_{hv} tended to be inversely correlated with the magnitude of D_{mh}. These associations occurred where ρ_{hv} rings were observed at temperatures between −5° and −20°C. The simulated ρ_{hv} rings marked areas of large hail, where it appeared that sedimentation along the periphery of the updraft increased D_{mh} through size sorting. The
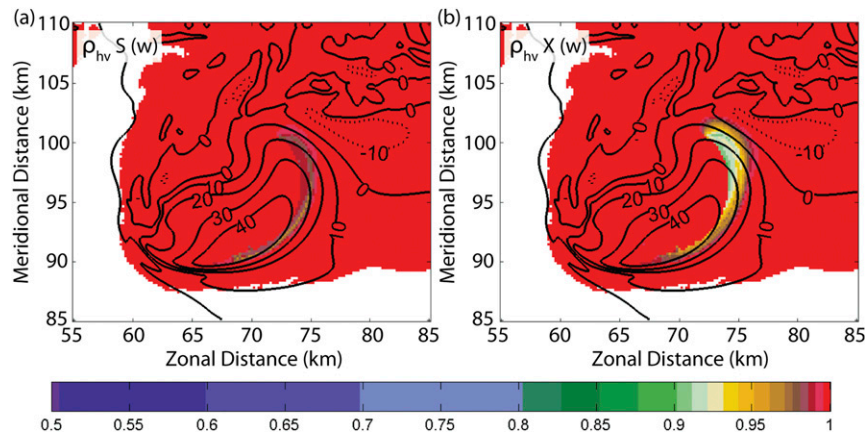
FIG. 11. Plots of ρ_{hv} (colors) at (a) S and (b) X bands from the 25q10 simulation at $t = 4080$ s and ~ 5600 m AGL. Contoured in black in (a) and (b) is w (m s^{-1}). The ρ_{hv} half ring is located along the eastern edge of the convective updraft and is considerably more apparent at X band than it is at S band.

simulations that produced the most intense updrafts and largest area of large hail also were associated with the largest and most robust ρ_{hv} rings. Similar to Jung et al. (2010), at heights close to the melting level, a reduction in ρ_{hv} was found in areas of mixed-phase precipitation (e.g., wet hail) owing to the diverse scattering behavior associated with a mixture of rain and wet hail.

Overall, the general location and structure of the simulated ρ_{hv} rings are similar to observed ρ_{hv} rings reported in the literature. For example, where the simulated rings are incomplete, they are located on the eastern (i.e., downshear) side of the updraft, similar to observations (e.g., Payne et al. 2010; KR08). In addition, there is a tendency for the magnitude of the depression in ρ_{hv} to be proportional to maximum hail size, with some simulations indicating a time lag in maximum correlation, again similar to observations (e.g., Picca and Ryzhkov 2012).

In simulations presented herein, ρ_{hv} is lower in magnitude than Jung et al. (2010) reported but higher in magnitude than seen in some X-band observations (e.g., Snyder et al. 2013). The former is primarily the result of scattering characteristics of hail at S band versus those at X band, whereas the latter is likely the result of more complicated scattering behaviors in nature that result from more exotic hydrometeor shapes, densities, and size distributions. The addition of two-layer T-matrix scattering calculations (e.g., Ryzhkov et al. 2011, 2013a,b) would be expected to improve the accuracy of the forward operator since it would better capture the scattering characteristics of mixed-phase hydrometeors that have a two-layer structure [such as hail undergoing wet growth or melting (e.g., Rasmussen et al. 1984)].

More high-quality, high-resolution observations of the midlevels of supercells are needed so that we can better compare these simulations with real-world observations.
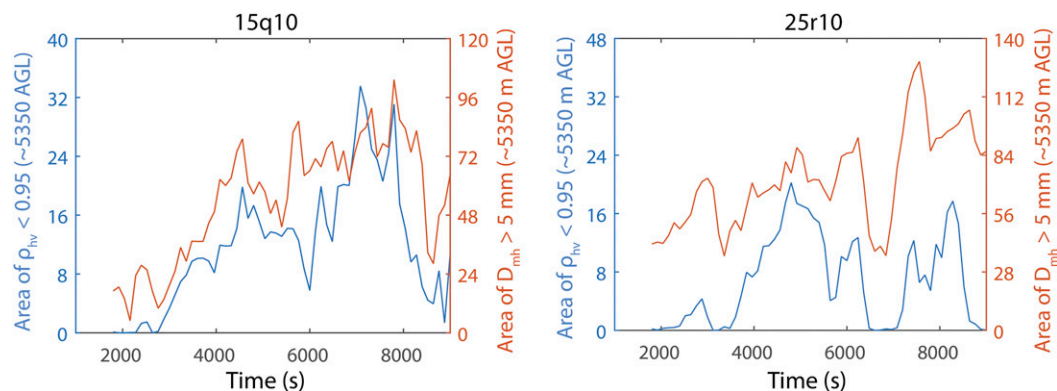

FIG. 12. Time series of the area of $\rho_{hv} < 0.95$ (blue line) and the area of $D_{mh} > 5$ mm (red line) in the (a) 15q10 and (b) 25r10 simulations. All data are valid at ~ 5350 m AGL and at X band.
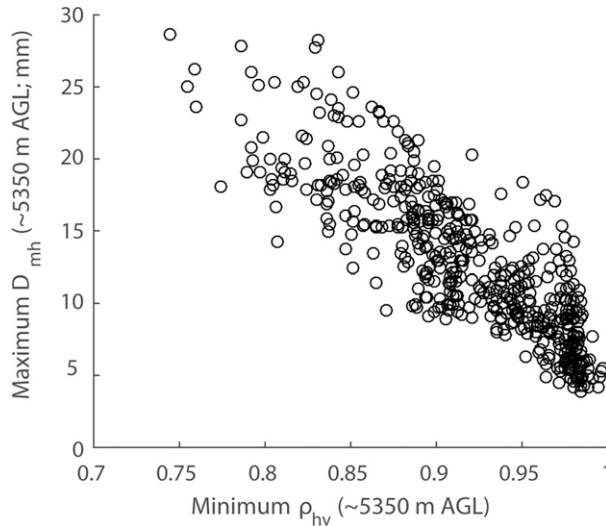
FIG. 13. A scatterplot of minimum ρ_{hv} and maximum D_{mh} (mm) at $\sim$5350 m AGL at each time in each simulation.

Many of the X-band radar observations of supercells have been collected by mobile radar deployed in field campaigns; such field campaigns often tended to prioritize the collection of low-level data. As such, there are relatively few datasets with high-quality, high-resolution polarimetric radar observations that have thorough coverage of the midlevels and upper levels (e.g., 4–12 km AGL) of supercells. Having such data with estimates of vertical velocity (as obtained, for example, through dual-Doppler wind synthesis) would greatly improve validation; with few exceptions (e.g., Jensen et al. 2016), such complete datasets do not exist. In addition, implementing more advanced attenuation estimation methods to mitigate the anomalously strong differential attenuation seen in the limited observations we do have would improve our ability to quantify the characteristics of these signatures at X band.

Despite the general observation that the polarimetric signatures examined in this paper and seen in supercells are captured by the model, more accurate representations of the signatures likely require microphysics that are more sophisticated than MY3. Bulk schemes, although more computationally efficient than spectral bin schemes, tend to be prone to error where a multimodal distribution would naturally occur, which can occur where different microphysical processes produce rain with distributions that are quite dissimilar. For example, rain resulting from shedding of hail undergoing wet growth tends to have different bulk characteristics than rain resulting from melting hail and from collision and coalescence, and the inability to capture this has ramifications for the accurate prediction of rain near the ground (e.g., Straka and Gilmore 2010; Van Den Broeke 2014;

Kumjian et al. 2015). The MY3 scheme only predicts a single rain category, and the densities for all hydrometeors are fixed; both of these are limitations that affect the representativeness of the simulated supercells with respect to those observed in nature. In addition, whereas MY3 predicts ice with fixed properties, at least one more recent scheme [predicted particle properties (P3); Morrison and Milbrandt 2015; Morrison et al. 2015; Milbrandt and Morrison 2016] predicts ice properties to allow for a more natural evolution of ice hydrometeors. Moreover, the liquid water fraction carried by graupel or hail that is undergoing wet growth or that is melting is not explicitly predicted in the MY3 scheme. Instead, this water fraction must be diagnosed, as is done in the PRFO used in this study. Future work may examine the impact of predicting water fraction within the microphysics scheme as compared with the diagnostic method used herein. Regardless, further development of the PRFO to handle more sophisticated scattering configurations is also warranted; for example, modeling wet hail as a water shell around an ice core as in Ryzhkov et al. (2011) is likely to improve the accuracy of simulated radar fields in areas of melting hail.

REFERENCES

Adlerman, E. J., and K. K. Droegemeier, 2002: The sensitivity of numerically simulated mesocyclogenesis to variations in model physics and computational parameters. *Mon. Wea. Rev.*, **130**, 2671–2691, doi:10.1175/1520-0493(2002)130<2671: TSONSC>2.0.CO;2.

——, and ——, 2005: The dependence of numerically simulated cyclic mesocyclogenesis upon environmental vertical wind shear. *Mon. Wea. Rev.*, **133**, 3595–3623, doi:10.1175/MWR3039.1.

Anagnostou, E. N., M. N. Anagnostou, W. F. Krajewski, A. Kruger, and B. J. Miriovsky, 2004: High-resolution rainfall estimation from X-band polarimetric radar measurements. *J. Hydrometeor.*, **5**, 110–128, doi:10.1175/1525-7541(2004)005<0110:HREFXP>2.0.CO;2.

——, M. Grecu, and M. N. Anagnostou, 2006: X-band polarimetric radar rainfall measurements in Keys Area Microphysics Project. *J. Atmos. Sci.*, **63**, 187–203, doi:10.1175/JAS3592.1.

Asefi-Najafabady, S., K. Knupp, U. Nair, J. Mecikalski, and R. Welch, 2010: Ground-based measurements and dual-Doppler analysis of 3-D wind fields and atmospheric circulations induced by a meso-γ-scale inland lake. *J. Geophys. Res.*, **115**, D23117, doi:10.1029/2010JD014022.

Aydin, K., and Y. Zhao, 1990: A computational study of polarimetric radar observables in hail. *IEEE Trans. Geosci. Remote Sens.*, **28**, 412–422, doi:10.1109/TGRS.1990.572906.

Bechini, R., L. Baldini, and V. Chandrasekar, 2013: Polarimetric radar observations in the ice region of precipitating clouds at C-band and X-band radar frequencies. *J. Appl. Meteor. Climatol.*, **52**, 1147–1169, doi:10.1175/JAMC-D-12-055.1.

Bharadwaj, N., K. Widener, K. Johnson, S. Collins, and A. Koontz, 2011: ARM radar infrastructure for global and regional climate study. *35th Conf. on Radar Meteorology*, Pittsburgh, PA, Amer. Meteor. Soc., 16B.4. [Available online at https://ams.confex.com/ams/35Radar/webprogram/Paper191707.html.]

Bluestein, H. B., M. M. French, R. L. Tanamachi, S. Frasier, K. Hardwick, F. Junyent, and A. L. Pazmany, 2007a: Close-range observations of tornadoes in supercells made with a dual-polarization, X-band, mobile Doppler radar. *Mon. Wea. Rev.*, **135**, 1522–1543, doi:10.1175/MWR3349.1.

——, C. C. Weiss, M. M. French, E. M. Holthaus, R. L. Tanamachi, S. Frasier, and A. L. Pazmany, 2007b: The structure of tornadoes near Attica, Kansas, on 12 May 2004: High-resolution, mobile, Doppler radar observations. *Mon. Wea. Rev.*, **135**, 475–506, doi:10.1175/MWR3295.1.

Borowska, L., A. V. Ryzhkov, D. S. Zrnić, C. Simmer, and R. Palmer, 2011: Attenuation and differential attenuation of 5-cm-wavelength radiation in melting hail. *J. Appl. Meteor. Climatol.*, **50**, 59–76, doi:10.1175/2010JAMC2465.1.

Brandes, E. A., G. Zhang, and J. Vivekanandan, 2002: Experiments in rainfall estimation with polarimetric radar in a subtropical environment. *J. Appl. Meteor.*, **41**, 674–685, doi:10.1175/1520-0450(2002)041<0674:EIREWA>2.0.CO;2; Corrigendum, **44**, 186, doi:10.1175/1520-0450(2005)44<186:C>2.0.CO;2.

Bringi, V. N., and V. Chandrasekar, 2001: *Polarimetric Doppler Weather Radar: Principles and Applications.* Cambridge University Press, 636 pp.

——, ——, N. Balakrishnan, and D. S. Zrnić, 1990: An examination of propagation effects in rainfall on radar measurements at microwave frequencies. *J. Atmos. Oceanic Technol.*, **7**, 829–840, doi:10.1175/1520-0426(1990)007<0829:AEOPEI>2.0.CO;2.

——, T. D. Keenan, and V. Chandrasekar, 2001: Correcting C-band radar reflectivity and differential reflectivity data for rain attenuation: A self-consistent method with constraints. *IEEE Trans. Geosci. Remote Sens.*, **39**, 1906–1915, doi:10.1109/36.951081.

Brooks, H. E., and R. B. Wilhelmson, 1993: Hodograph curvature and updraft intensity in numerically modeled supercells. *J. Atmos. Sci.*, **50**, 1824–1833, doi:10.1175/1520-0469(1993)050<1824:HCAUII>2.0.CO;2.

Browning, K. A., 1966: The lobe structure of giant hailstones. *Quart. J. Roy. Meteor. Soc.*, **92**, 1–14, doi:10.1002/qj.49709239102.

——, and J. G. D. Beimers, 1967: The oblateness of large hailstones. *J. Appl. Meteor.*, **6**, 1075–1081, doi:10.1175/1520-0450(1967)006<1075:TOOLH>2.0.CO;2.

Bryan, G. H., J. C. Wyngaard, and J. M. Fritsch, 2003: Resolution requirements for the simulation of deep moist convection. *Mon. Wea. Rev.*, **131**, 2394–2416, doi:10.1175/1520-0493(2003)131<2394:RRFTSO>2.0.CO;2.

Burgess, D. W., E. R. Mansell, C. M. Schwarz, and B. J. Allen, 2010: Tornado and tornadogenesis events seen by the NOXP X-band, dual-polarization radar during VORTEX2 2010. *25th Conf. on Severe Local Storms*, Denver, CO, Amer. Meteor. Soc., 5.2. [Available online at https://ams.confex.com/ams/25SLS/techprogram/paper_176164.htm.]

Carte, A. E., and R. E. Kidder, 1966: Transvaal hailstones. *Quart. J. Roy. Meteor. Soc.*, **92**, 382–391, doi:10.1002/qj.49709239307.

Cole, K. S., and R. H. Cole, 1941: Dispersion and absorption in dielectrics I: Alternating current characteristics. *J. Chem. Phys.*, **9**, 341–351, doi:10.1063/1.1750906.

Craven, J. P., and H. E. Brooks, 2004: Baseline climatology of sounding derived parameters associated with deep moist convection. *Natl. Wea. Dig.*, **28**, 13–24.

Dawson, D. T., II, M. Xue, J. A. Milbrandt, and M. K. Yau, 2010: Comparison of evaporation and cold pool development between single-moment and multimoment bulk microphysics schemes in idealized simulations of tornadic thunderstorms. *Mon. Wea. Rev.*, **138**, 1152–1171, doi:10.1175/2009MWR2956.1.

——, E. R. Mansell, Y. Jung, L. J. Wicker, M. R. Kumjian, and M. Xue, 2014: Low-level Z_{DR} signatures in supercell forward flanks: The role of size sorting and melting of hail. *J. Atmos. Sci.*, **71**, 276–299, doi:10.1175/JAS-D-13-0118.1.

——, M. Xue, J. Milbrandt, and A. Shapiro, 2015: Sensitivity of real-data simulations of the 3 May 1999 Oklahoma City tornadic supercell and associated tornadoes to multimoment microphysics. Part I: Storm- and tornado-scale numerical forecasts. *Mon. Wea. Rev.*, **143**, 2241–2265, doi:10.1175/MWR-D-14-00279.1.

——, ——, A. Shapiro, J. Milbrandt, and A. Schenkman, 2016: Sensitivity of real-data simulations of the 3 May 1999 Oklahoma City tornadic supercell and associated tornadoes to multimoment microphysics. Part II: Analysis of buoyancy and dynamic pressure forces in simulated tornado-like vortices. *J. Atmos. Sci.*, **73**, 1039–1061, doi:10.1175/JAS-D-15-0114.1.

Dolan, B., and S. A. Rutledge, 2009: A theory-based hydrometeor identification algorithm for X-band polarimetric radars. *J. Atmos. Oceanic Technol.*, **26**, 2071–2088, doi:10.1175/2009JTECHA1208.1.

Doviak, R. J., and D. S. Zrnić, 1993: *Doppler Radar and Weather Observations.* 2nd ed. Academic Press, 562 pp.

Ferrier, B. S., W.-K. Tao, and J. Simpson, 1995: A double-moment multiple-phase four-class bulk ice scheme. Part II: Simulations of convective storms in different large-scale environments and comparisons with other bulk parameterizations. *J. Atmos. Sci.*, **52**, 1001–1033, doi:10.1175/1520-0469(1995)052<1001:ADMMPF>2.0.CO;2.

Giammanco, I. M., T. M. Brown, M. R. Kumjian, and A. J. Heysmfield, 2014: Observations of hailstone sizes and shapes from the IBHS hail measurement program 2012–2014. *27th Conf. on Severe Local Storms*, Madison, WI, Amer. Meteor. Soc., 16B.2. [Available online at https://ams.confex.com/ams/27SLS/webprogram/Paper255294.html.]

Gorgucci, E., and V. Chandrasekar, 2005: Evaluation of attenuation correction methodology for dual-polarization radars: Application to X-band systems. *J. Atmos. Oceanic Technol.*, **22**, 1195–1206, doi:10.1175/JTECH1763.1.

Hubbert, J. C., and V. N. Bringi, 2000: The effects of three-body scattering on differential reflectivity signatures. *J. Atmos. Oceanic Technol.*, **17**, 51–61, doi:10.1175/1520-0426(2000)017<0051:TEOTBS>2.0.CO;2.

——, S. M. Ellis, M. Dixon, and G. Meymaris, 2010a: Modeling, error analysis, and evaluation of dual-polarization variables obtained from simultaneous horizontal and vertical polarization transmit radar. Part I: Modeling and antenna errors. *J. Atmos. Oceanic Technol.*, **27**, 1583–1598, doi:10.1175/2010JTECHA1336.1.

——, ——, ——, and ——, 2010b: Modeling, error analysis, and evaluation of dual-polarization variables obtained from simultaneous horizontal and vertical polarization transmit radar. Part II: Experimental data. *J. Atmos. Oceanic Technol.*, **27**, 1599–1607, doi:10.1175/2010JTECHA1337.1.

——, ——, W.-Y. Chang, and Y.-C. Liou, 2014: X-band polarimetric observations of cross coupling in the ice phase of convective storms in Taiwan. *J. Appl. Meteor. Climatol.*, **53**, 1678–1695, doi:10.1175/JAMC-D-13-0360.1.

Jensen, M. P., and Coauthors, 2016: The Midlatitude Continental Convective Clouds Experiment (MC3E). *Bull. Amer. Meteor. Soc.*, **97**, 1667–1686, doi:10.1175/BAMS-D-14-00228.1.

Johnson, M., Y. Jung, D. Dawson, and M. Xue, 2016: Comparison of simulated polarimetric signatures in idealized supercell storms using two-moment bulk microphysics schemes in WRF. *Mon. Wea. Rev.*, **144**, 971–996, doi:10.1175/MWR-D-15-0233.1.

Jung, Y., G. Zhang, and M. Xue, 2008: Assimilation of simulated polarimetric radar data for a convective storm using the ensemble Kalman filter. Part I: Observation operators for reflectivity and polarimetric variables. *Mon. Wea. Rev.*, **136**, 2228–2245, doi:10.1175/2007MWR2083.1.

——, M. Xue, and G. Zhang, 2010: Simulations of polarimetric radar signatures of a supercell storm using a two-moment bulk microphysics scheme. *J. Appl. Meteor. Climatol.*, **49**, 146–163, doi:10.1175/2009JAMC2178.1.

——, ——, and M. Tong, 2012: Ensemble Kalman filter analyses of the 29–30 May 2004 Oklahoma tornadic thunderstorms using one- and two-moment bulk microphysics schemes, with verification against polarimetric radar data. *Mon. Wea. Rev.*, **140**, 1457–1475, doi:10.1175/MWR-D-11-00032.1.

Junyent, F., V. Chandrasekar, P. Kennedy, S. Rutledge, V. Bringi, J. George, and D. Brunkow, 2013: Salient features of the CSU-CHILL radar X-band channel upgrade. *36th Conf. on Radar Meteorology*, Breckenridge, CO, Amer. Meteor. Soc., 2B.6. [Available online at https://ams.confex.com/ams/36Radar/webprogram/Paper229162.html.]

Kessler, E., 1969: *On the Distribution and Continuity of Water Substance in Atmospheric Circulations. Meteor. Monogr.*, No. 32, Amer. Meteor. Soc., 84 pp.

Klemp, J. B., and R. B. Wilhelmson, 1978: The simulation of three-dimensional convective storm dynamics. *J. Atmos. Sci.*, **35**, 1070–1096, doi:10.1175/1520-0469(1978)035<1070:TSOTDC>2.0.CO;2.

——, and R. Rotunno, 1983: A study of the tornadic region within a supercell thunderstorm. *J. Atmos. Sci.*, **40**, 359–377, doi:10.1175/1520-0469(1983)040<0359:ASOTTR>2.0.CO;2.

——, R. B. Wilhelmson, and P. S. Ray, 1981: Observed and numerically simulated structure of a mature supercell thunderstorm. *J. Atmos. Sci.*, **38**, 1558–1580, doi:10.1175/1520-0469(1981)038<1558:OANSSO>2.0.CO;2.

Knight, C. A., and N. C. Knight, 1970a: Lobe structures of hailstones. *J. Atmos. Sci.*, **27**, 667–671, doi:10.1175/1520-0469(1970)027<0667:LSOH>2.0.CO;2.

——, and ——, 1970b: The falling behavior of hailstones. *J. Atmos. Sci.*, **27**, 672–681, doi:10.1175/1520-0469(1970)027<0672:TFBOH>2.0.CO;2.

Knight, N. C., 1986: Hailstone shape factor and its relation to radar interpretation of hail. *J. Climate Appl. Meteor.*, **25**, 1956–1958, doi:10.1175/1520-0450(1986)025<1956:HSFAIR>2.0.CO;2.

Kumjian, M. R., 2013a: Principles and applications of dual-polarization weather radar. Part I: Description of the polarimetric radar variables. *J. Oper. Meteor.*, **1**, 226–242, doi:10.15191/nwajom.2013.0119.

——, 2013b: Principles and applications of dual-polarization weather radar. Part II: Warm- and cold-season applications. *J. Oper. Meteor.*, **1**, 243–264, doi:10.15191/nwajom.2013.0120.

——, 2013c: Principles and applications of dual-polarization weather radar. Part III: Artifacts. *J. Oper. Meteor.*, **1**, 265–274, doi:10.15191/nwajom.2013.0121.

——, and A. V. Ryzhkov, 2008: Polarimetric signatures in supercell thunderstorms. *J. Appl. Meteor. Climatol.*, **47**, 1940–1961, doi:10.1175/2007JAMC1874.1.

——, A. P. Khain, N. Benmoshe, E. Ilotoviz, A. V. Ryzhkov, and V. T. J. Phillips, 2014: The anatomy and physics of Z_{DR} columns: Investigating a polarimetric radar signature with a spectral bin microphysical model. *J. Appl. Meteor. Climatol.*, **53**, 1820–1843, doi:10.1175/JAMC-D-13-0354.1.

——, Z. J. Lebo, and H. C. Morrison, 2015: On the mechanisms of rain formation in an idealized supercell storm. *Mon. Wea. Rev.*, **143**, 2754–2773, doi:10.1175/MWR-D-14-00402.1.

Lin, Y.-L., R. D. Farley, and H. D. Orville, 1983: Bulk parameterization of the snow field in a cloud model. *J. Climate Appl. Meteor.*, **22**, 1065–1092, doi:10.1175/1520-0450(1983)022<1065:BPOTSF>2.0.CO;2.

Macklin, W. C., 1963: Heat transfer from hailstones. *Quart. J. Roy. Meteor. Soc.*, **89**, 360–369, doi:10.1002/qj.49708938107.

Maki, M., and Coauthors, 2008: X-band polarimetric radar network in the Tokyo metropolitan area—X-NET. *Proc. Fifth European Conf. on Radar in Meteorology and Hydrology*, Helsinki, Finland, Finnish Meteorological Institute, 3.7.

Mallet, C., and L. Barthes, 2009: Estimation of gamma raindrop size distribution parameters: Statistical fluctuations and estimation errors. *J. Atmos. Oceanic Technol.*, **26**, 1572–1584, doi:10.1175/2009JTECHA1199.1.

Mansell, E. R., C. L. Ziegler, and E. C. Bruning, 2010: Simulated electrification of a small thunderstorm with two-moment bulk microphysics. *J. Atmos. Sci.*, **67**, 171–194, doi:10.1175/2009JAS2965.1.

Maxwell Garnett, J. C., 1904: Colours in metal glasses and metal films. *Philos. Trans. Roy. Soc. London*, **203A**, 385–420, doi:10.1098/rsta.1904.0024.

McLaughlin, D., and Coauthors, 2009: Short-wavelength technology and the potential for distributed networks of small radar systems. *Bull. Amer. Meteor. Soc.*, **90**, 1797–1817, doi:10.1175/2009BAMS2507.1.

Meyers, M. P., R. L. Walko, J. Y. Harrington, and W. R. Cotton, 1997: New RAMS cloud microphysics parameterization. Part II: The two-moment scheme. *Atmos. Res.*, **45**, 3–39, doi:10.1016/S0169-8095(97)00018-5.

Milbrandt, J. A., and M. K. Yau, 2005a: A multimoment bulk microphysics parameterization. Part I: Analysis of the role of the spectral shape parameter. *J. Atmos. Sci.*, **62**, 3051–3064, doi:10.1175/JAS3534.1.

——, and ——, 2005b: A multimoment bulk microphysics parameterization. Part II: A proposed three-moment closure and scheme description. *J. Atmos. Sci.*, **62**, 3065–3081, doi:10.1175/JAS3535.1.

——, and R. McTaggart-Cowan, 2010: Sedimentation-induced errors in bulk microphysics schemes. *J. Atmos. Sci.*, **67**, 3931–3948, doi:10.1175/2010JAS3541.1.

——, and H. Morrison, 2016: Parameterization of cloud microphysics based on the prediction of bulk ice particle properties. Part III: Introduction of multiple free categories. *J. Atmos. Sci.*, **73**, 975–995, doi:10.1175/JAS-D-15-0204.1.

Morrison, H., and J. Milbrandt, 2015: Parameterization of cloud microphysics based on the prediction of bulk ice particle properties. Part I: Scheme description and idealized tests. *J. Atmos. Sci.*, **72**, 287–311, doi:10.1175/JAS-D-14-0065.1.

——, J. A. Curry, and V. I. Khvorostyanov, 2005: A new double-moment microphysics parameterization for application in cloud and climate models. Part I: Description. *J. Atmos. Sci.*, **62**, 1665–1677, doi:10.1175/JAS3446.1.

——, J. Milbrandt, G. Bryan, K. Ikeda, S. Tessendorf, and G. Thompson, 2015: Parameterization of cloud microphysics based on the prediction of bulk ice particle properties. Part II: Case study comparisons with observations and other schemes. *J. Atmos. Sci.*, **72**, 312–339, doi:10.1175/JAS-D-14-0066.1.

National Climatic Data Center, 2013: *Storm Data*, Vol. 55, No. 4, 363 pp. [Available online at https://www.ncdc.noaa.gov/IPS/sd/sd.html.]

Park, S.-G., V. N. Bringi, V. Chandrasekar, M. Maki, and K. Iwanami, 2005a: Correction of radar reflectivity and differential reflectivity for rain attenuation at X band. Part I: Theoretical and empirical basis. *J. Atmos. Oceanic Technol.*, **22**, 1621–1631, doi:10.1175/JTECH1803.1.

——, M. Maki, K. Iwanami, V. N. Bringi, and V. Chandrasekar, 2005b: Correction of radar reflectivity and differential reflectivity for rain attenuation at X band. Part II: Evaluation and application. *J. Atmos. Oceanic Technol.*, **22**, 1633–1655, doi:10.1175/JTECH1804.1.

Payne, C. D., T. J. Schuur, D. R. MacGorman, M. I. Biggerstaff, K. M. Kuhlman, and W. D. Rust, 2010: Polarimetric and electrical characteristics of a lightning ring in a supercell storm. *Mon. Wea. Rev.*, **138**, 2405–2425, doi:10.1175/2009MWR3210.1.

Pazmany, A. L., J. B. Mead, H. B. Bluestein, J. C. Snyder, and J. B. Houser, 2013: A mobile rapid-scanning polarimetric (RaXPol) Doppler radar system. *J. Atmos. Oceanic Technol.*, **30**, 1398–1413, doi:10.1175/JTECH-D-12-00166.1.

Pereira Filho, A. J., O. Massambani, R. Hallak, C. Beneti, and R. B. Gin, 2007: MXPOL measurements of weather systems. *33rd Conf. on Radar Meteorology*, Cairns, Australia, Amer. Meteor. Soc., 8A.5. [Available online at https://ams.confex.com/ams/33Radar/techprogram/paper_123393.htm.]

Petch, J. C., 2006: Sensitivity studies of developing convection in a cloud-resolving model. *Quart. J. Roy. Meteor. Soc.*, **132**, 345–358, doi:10.1256/qj.05.71.

Pfeifer, M., G. C. Craig, M. Hagen, and C. Keil, 2008: A polarimetric radar forward operator for model evaluation. *J. Appl. Meteor. Climatol.*, **47**, 3202–3220, doi:10.1175/2008JAMC1793.1.

Picca, J. C., and A. V. Ryzhkov, 2012: A dual-wavelength polarimetric analysis of the 16 May 2010 Oklahoma City extreme hailstorm. *Mon. Wea. Rev.*, **140**, 1385–1403, doi:10.1175/MWR-D-11-00112.1.

Posselt, D. J., X. Li, S. A. Tushaus, and J. R. Mecikalski, 2015: Assimilation of dual-polarization radar observations in mixed- and ice-phase regions of convective storms: Information content and forward model errors. *Mon. Wea. Rev.*, **143**, 2611–2636, doi:10.1175/MWR-D-14-00347.1.

Rasmussen, E. N., 2003: Refined supercell and tornado forecast parameters. *Wea. Forecasting*, **18**, 530–535, doi:10.1175/1520-0434(2003)18<530:RSATFP>2.0.CO;2.

——, and D. O. Blanchard, 1998: A baseline climatology of sounding-derived supercell and tornado forecast parameters. *Wea. Forecasting*, **13**, 1148–1164, doi:10.1175/1520-0434(1998)013<1148:ABCOSD>2.0.CO;2.

Rasmussen, R. M., and A. J. Heymsfield, 1987: Melting and shedding of graupel and hail. Part I: Model physics. *J. Atmos. Sci.*, **44**, 2754–2763, doi:10.1175/1520-0469(1987)044<2754:MASOGA>2.0.CO;2.

——, V. Levizzani, and H. R. Pruppacher, 1984: A wind tunnel and theoretical study on the melting behavior of atmospheric ice particles: III. Experiment and theory for spherical ice particles of radius $> 500\,\mu m$. *J. Atmos. Sci.*, **41**, 381–388, doi:10.1175/1520-0469(1984)041<0381:AWTATS>2.0.CO;2.

Reisner, J., R. M. Rasmussen, and R. T. Bruintjes, 1998: Explicit forecasting of supercooled liquid water in winter storms using the MM5 mesoscale model. *Quart. J. Roy. Meteor. Soc.*, **124**, 1071–1107, doi:10.1002/qj.49712454804.

Rotunno, R., 1981: On the evolution of thunderstorm rotation. *Mon. Wea. Rev.*, **109**, 577–586, doi:10.1175/1520-0493(1981)109<0577:OTEOTR>2.0.CO;2.

——, and J. B. Klemp, 1982: The influence of the shear-induced pressure gradient on thunderstorm motion. *Mon. Wea. Rev.*, **110**, 136–151, doi:10.1175/1520-0493(1982)110<0136:TIOTSI>2.0.CO;2.

——, and ——, 1985: On the rotation of propagation of simulated supercell thunderstorms. *J. Atmos. Sci.*, **42**, 271–292, doi:10.1175/1520-0469(1985)042<0271:OTRAPO>2.0.CO;2.

Ryzhkov, A. V., 2007: The impact of beam broadening on the quality of radar polarimetric data. *J. Atmos. Oceanic Technol.*, **24**, 729–744, doi:10.1175/JTECH2003.1.

——, and D. S. Zrnić, 2007: Depolarization in ice crystals and its effect on radar polarimetric measurements. *J. Atmos. Oceanic Technol.*, **24**, 1256–1267, doi:10.1175/JTECH2034.1.

——, P. Zhang, D. Hudak, J. L. Alford, M. Knight, and J. W. Conway, 2007: Validation of polarimetric methods for attenuation correction at C band. *33rd Conf. on Radar Meteorology*, Cairns, Australia, Amer. Meteor. Soc., 11B.12. [Available online at https://ams.confex.com/ams/33Radar/techprogram/paper_123122.htm.]

——, M. Pinsky, A. Pokrovsky, and A. Khain, 2011: Polarimetric radar observation operator for a cloud model with spectral microphysics. *J. Appl. Meteor. Climatol.*, **50**, 873–894, doi:10.1175/2010JAMC2363.1.

——, M. R. Kumjian, S. M. Ganson, and A. P. Khain, 2013a: Polarimetric radar characteristics of melting hail. Part I: Theoretical simulations using spectral microphysical modeling. *J. Appl. Meteor. Climatol.*, **52**, 2849–2870, doi:10.1175/JAMC-D-13-073.1.

——, ——, ——, and P. Zhang, 2013b: Polarimetric radar characteristics of melting hail. Part II: Practical implications. *J. Appl. Meteor. Climatol.*, **52**, 2871–2886, doi:10.1175/JAMC-D-13-074.1.

Seifert, A., and K. D. Beheng, 2006: A two-moment cloud microphysical parameterization for mixed-phase clouds. Part 1: Model description. *Meteor. Atmos. Phys.*, **92**, 45–66, doi:10.1007/s00703-005-0112-4.

Smyth, T. J., and A. J. Illingworth, 1998: Correction for attenuation of radar reflectivity using polarization data. *Quart. J. Roy. Meteor. Soc.*, **124**, 2393–2415, doi:10.1002/qj.49712455111.

Snyder, J. C., H. B. Bluestein, G. Zhang, and S. F. Frasier, 2010: Attenuation correction and hydrometeor classification of high-resolution, X-band, dual-polarized mobile radar measurements in severe convective storms. *J. Atmos. Oceanic Technol.*, **27**, 1979–2001, doi:10.1175/2010JTECHA1356.1.

——, ——, V. Venkatesh, and S. J. Frasier, 2013: Observations of polarimetric signatures in supercells by an X-band mobile

Doppler radar. *Mon. Wea. Rev.*, **141**, 3–29, doi:10.1175/MWR-D-12-00068.1.

——, A. V. Ryzhkov, M. R. Kumjian, A. Khain, and J. C. Picca, 2015: A Z_{DR} column detection algorithm to examine convective storm updrafts. *Wea. Forecasting*, **30**, 1819–1844, doi:10.1175/WAF-D-15-0068.1.

——, H. B. Bluestein, D. T. Dawson II, and Y. Jung, 2017: Simulations of polarimetric, X-band radar signatures in supercells. Part II: Z_{DR} columns and rings and K_{DP} columns. *J. Appl. Meteor. Climatol.*, **56**, 2001–2026, doi:10.1175/JAMC-D-16-0139.1.

Straka, J. M., 2009: *Cloud and Precipitation Microphysics: Principles and Parameterizations.* Cambridge University Press, 392 pp.

——, and M. S. Gilmore, 2010: A novel, multiple liquid and ice hydrometeor species, hybrid-bulk/bin, three-moment microphysics parameterization scheme. *13th Conf. on Cloud Physics*, Portland, OR, Amer. Meteor. Soc., 2.3. [Available online at https://ams.confex.com/ams/13CldPhy13AtRad/webprogram/Paper171873.html.]

——, D. S. Zrnić, and A. V. Ryzhkov, 2000: Bulk hydrometeor classification and quantification using polarimetric radar data: Synthesis of relations. *J. Appl. Meteor.*, **39**, 1341–1372, doi:10.1175/1520-0450(2000)039<1341:BHCAQU>2.0.CO;2.

Testud, J., E. Le Bouar, E. Obligis, and M. Ali-Mehenni, 2000: The rain profiling algorithm applied to polarimetric weather radar. *J. Atmos. Oceanic Technol.*, **17**, 332–356, doi:10.1175/1520-0426(2000)017<0332:TRPAAT>2.0.CO;2.

Thompson, R. L., R. Edwards, J. A. Hart, K. L. Elmore, and P. Markowski, 2003: Close proximity soundings within supercell environments obtained from the Rapid Update Cycle. *Wea. Forecasting*, **18**, 1243–1261, doi:10.1175/1520-0434(2003)018<1243:CPSWSE>2.0.CO;2.

Ulbrich, C. W., 1983: Natural variations in the analytical form of the raindrop size distribution. *J. Climate Appl. Meteor.*, **22**, 1764–1775, doi:10.1175/1520-0450(1983)022<1764:NVITAF>2.0.CO;2.

Van Den Broeke, M. S., 2014: Effects of mid- and upper-level dry layers on microphysics of simulated supercell storms. *Electron. J. Severe Storms Meteor.*, **9**, 3. [Available online at http://www.ejssm.org/ojs/index.php/ejssm/article/viewFile/134/99.]

——, J. M. Straka, and E. N. Rasmussen, 2010: Mesocyclone and RFD evolution in simulated supercell storms with varying wind profiles. 25th Conf. on Severe Local Storms, Denver, CO, Amer. Meteor. Soc., 8A.6. [Available online at https://ams.confex.com/ams/25SLS/webprogram/Paper175853.html.]

Vivekanandan, J., V. N. Bringi, and R. Raghavan, 1990: Multiparameter radar modeling and observations of melting ice. *J. Atmos. Sci.*, **47**, 549–564, doi:10.1175/1520-0469(1990)047<0549:MRMAOO>2.0.CO;2.

——, W. M. Adams, and V. N. Bringi, 1991: Rigorous approach to polarimetric radar modeling of hydrometeor orientation

distributions. *J. Appl. Meteor.*, **30**, 1053–1063, doi:10.1175/1520-0450(1991)030<1053:RATPRM>2.0.CO;2.

Weisman, M. L., and J. B. Klemp, 1982: The dependence of numerically simulated convective storms on vertical wind shear and buoyancy. *Mon. Wea. Rev.*, **110**, 504–520, doi:10.1175/1520-0493(1982)110<0504:TDONSC>2.0.CO;2.

——, and ——, 1984: The structure and classification of numerically simulated convective storms in directionally varying wind shears. *Mon. Wea. Rev.*, **112**, 2479–2498, doi:10.1175/1520-0493(1984)112<2479:TSACON>2.0.CO;2.

Wicker, L. J., and R. B. Wilhelmson, 1995: Simulation and analysis of tornado development and decay within a three-dimensional supercell thunderstorm. *J. Atmos. Sci.*, **52**, 2675–2703, doi:10.1175/1520-0469(1995)052<2675:SAAOTD>2.0.CO;2.

Wilson, J. W., and D. Reum, 1988: The flare echo: Reflectivity and velocity signature. *J. Atmos. Oceanic Technol.*, **5**, 197–205, doi:10.1175/1520-0426(1988)005<0197:TFERAV>2.0.CO;2.

Wurman, J., K. Kosiba, P. Robinson, and T. Marshall, 2014: The role of multiple vortex tornado structure in causing storm researcher fatalities. *Bull. Amer. Meteor. Soc.*, **95**, 31–45, doi:10.1175/BAMS-D-13-00221.1.

Xue, M., K. K. Droegemeier, and V. Wong, 2000: The Advanced Regional Prediction System (ARPS)—A multi-scale nonhydrostatic atmospheric simulation and prediction tool. Part I: Model dynamics and verification. *Meteor. Atmos. Phys.*, **75**, 161–193, doi:10.1007/s007030070003.

——, and Coauthors, 2001: The Advanced Regional Prediction System (ARPS)—A multi-scale nonhydrostatic atmospheric simulation and prediction tool. Part II: Model physics and applications. *Meteor. Atmos. Phys.*, **76**, 143–165, doi:10.1007/s007030170027.

——, D.-H. Wang, J.-D. Gao, K. Brewster, and K. K. Droegemeier, 2003: The Advanced Regional Prediction System (ARPS), storm-scale numerical weather prediction and data assimilation. *Meteor. Atmos. Phys.*, **82**, 139–170.

Ziegler, C. L., 1985: Retrieval of thermal and microphysical variables in observed convective storms. Part I: Model development and preliminary testing. *J. Atmos. Sci.*, **42**, 1487–1509, doi:10.1175/1520-0469(1985)042<1487:ROTAMV>2.0.CO;2.

Zrnić, D. S., 1987: Three-body scattering produces precipitation signature of special diagnostic value. *Radio Sci.*, **22**, 76–86, doi:10.1029/RS022i001p00076.

——, and A. V. Ryzhkov, 1996: Advantages of rain measurements using specific differential phase. *J. Atmos. Oceanic Technol.*, **13**, 454–464, doi:10.1175/1520-0426(1996)013<0454:AORMUS>2.0.CO;2.

——, and ——, 1999: Polarimetry for weather surveillance radars. *Bull. Amer. Meteor. Soc.*, **80**, 389–406, doi:10.1175/1520-0477(1999)080<0389:PFWSR>2.0.CO;2.